The Paris Climate Agreement and future sea level rise from Antarctica

*Robert M. DeConto[1], David Pollard[2], Richard B. Alley[2,3], Isabella Velicogna[4], Edward Gasson[5], Natalya Gomez[6], Shaina Sadai[1], Alan Condron[7], Daniel M. Gilford[8], Erica L. Ashe[8], Robert E. Kopp[8], Dawei Li[1], and Andrea Dutton[9]

[1]Department of Geosciences, University of Massachusetts Amherst, Amherst, Massachusetts 01003, USA, deconto@geo.umass.edu

[2]Earth and Environmental Systems Institute, Pennsylvania State University, University Park, Pennsylvania 16802, USA

[3]Department of Geosciences, Pennsylvania State University, University Park, Pennsylvania 16802, USA

[4]Earth System Science, University of California, Irvine, CA, USA, 92697, Isabella@uci.edu

[5]School of Geographical Sciences, University of Bristol, Clifton, Bristol BS8 1SS UK

[6]Department of Earth and Planetary Sciences, McGill University, Montreal, Quebec, Canada, H3A 0E

[7]Department of Geology and Geophysics, Woods Hole Oceanographic Institution, Woods Hole, MA 02543, USA

[8]Department of Earth and Planetary Sciences, Rutgers University, Piscataway, NJ 08854

[9]Department of Geoscience, University of Wisconsin-Madison, Madison, WI 53706

The Paris Agreement aims to limit global mean warming in the 21st century to less than 2 ºC above preindustrial levels, and to promote further efforts to limit the warming to 1.5 ºC. Here, we use an observationally calibrated ice sheet-shelf model including ductile and brittle processes that can initiate dynamic instabilities, to test Antarctica's response to future climate scenarios representing Paris Agreement aspirations versus more fossil-fuel intensive emissions scenarios. We find that global mean warming above 2 ºC substantially increases the risk of triggering rapid ice-sheet retreat, initiated by the thinning and loss of Antarctic ice shelves. A scenario consistent with current policies and allowing +3 ºC of warming by 2100 causes an abrupt jump in the pace of ice loss after ~2060, equivalent to ~0.5 cm sea level rise per year. Once initiated, rapid Antarctic ice loss continues for centuries, regardless of bedrock/sea level feedbacks or geoengineered carbon dioxide reduction (CDR). These results demonstrate the possibility that unstoppable, catastrophic sea level rise from Antarctica will be triggered if Paris Agreement temperature targets are exceeded.

Greenland is currently losing ice at a faster pace than Antarctica[1,2], but Antarctica contains almost eight (7.74) times more ice above floatation, equivalent to 58 m of global mean sea level (GMSL)[3]. The Antarctic Ice Sheet (AIS) is fundamentally different from the Greenland Ice Sheet, because most of its margin terminates directly in the surrounding ocean, with massive ice shelves (floating extensions of glacial ice) providing resistance (buttressing) to the seaward flow of the grounded ice upstream[4]. About a third of the AIS rests on bedrock hundreds to thousands of meters below sea level[3] and in places where subglacial bedrock slopes downward away from the ocean (reverse-sloped), the ice margin is susceptible to dynamical instabilities; the *Marine Ice-Sheet Instability* (MISI)[5,6] and possibly a *Marine Ice-Cliff Instability* (MICI)[7,8] that can drive rapid retreat. The West Antarctic Ice Sheet (WAIS), with the potential to cause ~5 m of sea level rise[3], is particularly vulnerable. WAIS is currently losing ice faster than other sectors of the AIS[1], and it sits in a deep, bowl-shaped basin >2.5 km below sea level in places.

Marine ice sheet instabilities triggered by the loss of ice shelves

Both MISI and MICI can be triggered by the thinning or loss of buttressing ice shelves in response to a warming ocean, atmosphere, or both[9]. MISI is related to a self-sustaining positive feedback between seaward ice flux across the grounding line (the boundary between grounded and floating ice) and ice thickness[5,6]. If buttressing is lost and retreat is initiated on a reverse-sloped bed, the retreating grounding line will encounter thicker ice, strongly increasing seaward ice flow. Retreat will continue until the grounding line reaches forward-sloping bedrock, or sufficient resistive stress is restored by the regrowth of a buttressing ice shelf confined within coastal embayments or thick enough to 'pin' on shallow bedrock features. Thus, grounding lines on reverse-sloped bedrock are conditionally unstable[10] with instability or stability determined by the complex interplay between ice flow and stress fields, bedrock conditions, surface mass balance, and other factors that make modeling these dynamics difficult.

MICI is also theorized to be triggered where buttressing ice shelves are lost or become too small to provide substantial back stress[7,8]. If the ice thickness exceeds a critical value, the weight of the ice above sea level produces deviatoric stresses at the unsupported grounding line that can exceed the material yield strength of the ice, and the ice fails structurally[11,12]; possibly manifest as repeated ice-cliff slumping and calving events[12]. Once initiated, failure could continue until the collapsing ice front backs into shallow water where cliff heights and the associated stresses drop below their critical values, or sufficient buttressing support is restored by an ice shelf.

In undamaged ice, with small grain sizes and without large bubbles or preexisting weaknesses, slowly emerging subaerial ice cliffs could exceed 500 m in height before failing[11-13]. However, natural glacial ice outside the laboratory is typically heavily damaged, especially near crevassed calving fronts and in fast-flowing ice upstream[14]. Assuming properties more representative of natural ice, stress balance calculations[11] point to maximum sustainable cliff heights of around 200 m. This value is reduced to ~100 m or less[8,11] where deep surface and basal crevasses effectively thin the supportive ice column (increasing the stress), which may explain why the tallest subaerial ice cliffs observed today are ~100 m tall. Recent modelling[13] using values of fracture toughness and preexisting flaw size considered appropriate for damaged ice fronts[12] and consistent with field observations[14] indicates tensile fracturing can occur at cliffs as low as 60 m, reinforcing why ice-cliff calving should be included in ice sheet models[15], despite ongoing uncertainties in ice properties and the lack of observations that has made mechanistic ice-cliff calving laws difficult to formulate.

Thick, marine-terminating glaciers such as Jakobshavn Isbræ in Greenland demonstrate how efficiently calving can deliver ice to the ocean. The terminus of Jakobshavn is ~10 km wide, ~1000 m thick, and flowing seaward at ~12 km yr^{-1} [16]. Since the glacier lost its ice shelf in the late 1990s, the ice front (with an intermittent ~100 m ice cliff) has retreated >12 km into the thicker ice upstream, albeit with a recent re-advance coincident with regional ocean cooling[17]. The average effective calving rate (flow speed + retreat) between 2002 and 2015 is estimated at 13.2 ± 0.9 km yr^{-1} [16].

Calving in narrow fjord settings like Jakobshavn is controlled by a complex combination of ductile and brittle processes, and buoyancy. After a calving event, subsequent fracture-driven failure is delayed until accelerated flow thins the ice front to near-flotation, allowing tidal flexure, basal crevassing, slumping, or other processes to initiate the next event[18,19]. Resistive stresses from lateral shear along the fjord walls, and thick mélange strengthened by seasonal sea ice slows the calving in winter, but the annual rate of ice loss remains high.

Fast-paced calving like that at Jakobshavn is not widespread in Antarctica today, because most marine-terminating grounding lines with comparable ice thickness are supported by the resistive backstress of ice shelves. Crane Glacier, previously buttressed by the Larsen B ice shelf on the Antarctic Peninsula is an exception. When the ice shelf suddenly collapsed in 2002 after becoming covered in meltwater, the glacier sped up by a factor of 3[20]. A persistent 100-meter tall ice cliff formed at the terminus[21] and the calving front retreated into its narrow fjord. Crane Glacier and its drainage were too small to contribute substantially to sea level. However, if Antarctic ocean and air temperatures continue to rise, the sequence of events that played out at Crane Glacier could become more widespread.

Importantly, the spatial scale of some Antarctic glaciers is vastly larger than their Greenland counterparts. For example, Thwaites Glacier in West Antarctica flows into the open Amundsen Sea rather than a narrow fjord. Thwaite's main trunk is about 120 km wide, it widens upstream, and it drains the heart of the WAIS. Today, the heavily crevassed Thwaites grounding zone is minimally buttressed and retreating on reverse-sloped bedrock at >1 km yr^{-1} in places[22] possibly due to dynamics associated with MISI. The terminus currently sits in water too shallow (~600 m deep) to produce an unstable cliff face. However, at its current rate of retreat into deeper bedrock and thicker ice, Thwaites could soon have a calving face taller than Jakobshavn, with stresses and strain rates exceeding thresholds for brittle failure[11-13]. Similar vulnerabilities exist at other Antarctic glaciers, particularly where buttressing ice shelves are already in a state of decline from contact with warm sub-surface waters[9].

Because of the very strong dependency of crack growth with increasing stress[12,23], a previously unseen style of calving and ice failure might emerge at Antarctic ice fronts with thicker unbuttressed ice, higher freeboard, and greater stresses than glaciers on Greenland[7,8]. The potential pace of fracturing in such high-stress settings remains uncertain[15] but once a calving front backs into thicker ice upstream, brittle failure could outpace viscous flow, inhibiting the growth of a new shelf. Complete and sustained loss of an ice shelf exposing a grounding-line cliff is not a necessary condition for structural failure[11]. If a small floating ice shelf were to survive or reform without providing substantial buttressing, the grounding zone would remain under sufficient stress for collapse. Any reemerging ice shelves would be vulnerable to warm ocean waters and surface meltwater, and likely to remain small. Jakobshavn and Crane Glacier provide evidence of this; despite fast flow and mélange buttressing they have not been able to reform extensive ice tongues and calving continues.

Extensive loss of buttressing ice shelves (key prerequisite for MISI and MICI) represents a possible tipping point in Antarctica's future. This is concerning, because ice shelves are vulnerable to both oceanic melt from below[9] and surface warming from above[24]. Rain and meltwater can deepen crevasses[24] and cause flexural stresses[25] that can lead to hydrofracturing and ice-shelf collapse. Vulnerability to surface meltwater is enhanced where firn (the transitional layer between surface snow and underlying ice) becomes saturated, and where ocean-driven thinning is already underway[24]. Air temperatures above Antarctica's largest buttressing ice shelves are currently too cold to produce sustained rates of meltwater associated with collapse[26,27]; however, given sufficient future warming, this situation could change.

Modeling the Antarctic Ice Sheet's response to climate change

We build on previous work[8] by improving a hybrid ice sheet-shelf model that includes viscous ice processes related to MISI and brittle processes related to MICI. The model allows conditionally unstable grounding-line (MISI) behavior on reverse sloped bedrock in response to flow and stress fields, bed conditions, and surface mass balance. The model accounts for oceanic sub-ice melt and meltwater-driven hydrofracturing of ice shelves, leading to structural failure (ice-cliff calving) at thick, marine-terminating ice fronts where stresses are diagnosed to exceed the material strength of ice (MICI). Model improvements and extensions described in Methods and Supplementary Information include new formulations of ice-shelf buttressing, hydrofracturing, coupling with a comprehensive Earth-sea level model, and the inclusion of ice-climate (meltwater) feedbacks using the NCAR Community Earth System Model. Parametric uncertainty is assessed using modern and geologic observations and statistical emulation. Regional climate model (RCM) forcing used in future ice sheet ensembles is substantially improved relative to ref.[8], with the timing and magnitude of warming comparable to other studies[26] (Supplementary Information).

The model is used to test the future response of the AIS to scenarios representing +1.5 ºC and +2º C global warming limits[28], a +3 ºC scenario representing current policies[29], and extended RCP emissions scenarios[30]. We consider recently proposed negative feedbacks that could slow the pace of future ice loss, and emissions scenarios that allow a temporary overshoot of Paris Agreement temperature targets followed by rapid CDR, assuming such geoengineering is possible. The results identify emissions-forced climatic thresholds capable of triggering rapid retreat of the AIS.

Calibrated Antarctic Ice Sheet ensembles

To account for ongoing uncertainty in key physical parameters controlling 1) the sensitivity of crevasse penetration to surface melt and rainwater (hydrofracturing) and 2) the maximum rate of ice-cliff calving, 196 ice-sheet simulations are run for each climate scenario described below. Each ensemble member uses a unique combination of hydrofracturing and cliff-calving parameter values (Extended Data Table 1). Parameter combinations are scored using a binary history-matching approach[8,31], based on their ability to simulate 1) the average rate of observed ice loss $\frac{d\bar{M}}{dt}$ between 1992 and 2017 (IMBIE)[1], 2) Antarctica's contribution to Last Interglacial (LIG) sea level[32], and 3) Antarctica's contribution to mid Pliocene sea level[33,34] (Methods). Ensemble members that fall outside the likely range of the observational constraints are discarded and only those parameter combinations within the bounds of all three constraints are included in projections of future ice loss. Both modern and geological constraints contain considerable uncertainty with poorly known sample distributions, so weighting of individual model outcomes is avoided. This method of ensemble scoring is compared to a more rigorous Gaussian Process emulation approach similar to that in ref.[31], to verify that the central estimates of our calibrated ensembles are robust (Supplementary Information).

Comparing simulated and IMBIE estimates of $\frac{d\bar{M}}{dt}$ (Extended Data Figure 1) eliminates 33 ensemble members (n=163). Replacing IMBIE with alternative (narrower) ranges of $\frac{d\bar{M}}{dt}$ based solely on Gravity Recovery and Climate Experiment (GRACE) data between 2002-2017[35] (Methods) eliminates more ensemble members than IMBIE but increases projections of future ice loss (Extended Data Figure 2). We use the longer and more conservative IMBIE record as our default training constraint.

The model performs well over the IMBIE interval with and without hydrofracturing and ice-cliff calving enabled (Extended Data Figure 1a). While IMBIE provides some guidance on processes causing contemporary mass change (surface mass balance, sub-ice shelf thinning, and grounding line dynamics), it does not sufficiently test the brittle ice processes theorized to become important in a warmer climate[7,8]. Furthermore, the 25-year IMBIE record is very short relative to the dynamical response time of an ice sheet and interdecadal and longer variability is not captured. Collectively, these issues motivate our use of geological records from past warm periods as additional training constraints.

Adding the LIG constraint (3.1-6.1 m between 129 ka and 128 ka)[32] to IMBIE eliminates an additional 44 parameter combinations (n=119), but only at the lower bound of the parameter range (Extended Data Figure 1b). Without MICI, the model is incapable of simulating realistic LIG ice loss. Even at the top of the parameter range, simulated rates of GMSL rise during the early LIG remain below 1 cm yr^{-1} (Extended Data Figure 1c), slower than indicated by some proxy records[36].

Adding a warm mid-Pliocene (3.3-3.0 Ma) test with a target range of 11-21 m (Methods) further reduces the ensemble to n=109 by eliminating some of the highest valued parameter combinations. However, like the LIG, we find that substantial hydrofracturing and ice-cliff calving must be included to satisfy Pliocene geological observations (Extended Data Figure 1b,d), including the magnitude of ice loss[33,34] and regional retreat into East Antarctic basins[37] (Extended Data Figure 3).

The ability of the model to simulate current rates of ice loss without ice-cliff calving, while failing to simulate past examples of retreat under warm climate conditions (Extended Data Figure 1) is at odds with the findings of ref.[31] and illustrates the importance of paleoclimate records for model validation. Model processes other than ice-cliff calving can increase the sensitivity of ice sheet models to a given forcing. For example, Pliocene retreat in East Antarctica has been simulated in an ice sheet model without MICI, using a sub-ice melt scheme that allows melt beneath grounded ice upstream of the grounding line[38]. Tidally driven seawater intrusion and non-zero melt beneath laterally discontinuous sectors of grounding zones have been observed[22], however model treatments used to date[38] have been questioned on physical grounds[39], and it remains unclear if such processes alone can account for the pace of past ice loss seen in geologic records. Alternative (Coulomb) sub-glacial sliding laws have been proposed[40] that can substantially increase the pace of ice loss in ice flow models with ice shelves removed[41], but these models have not been tested with realistic paleoclimate forcing. We stress that the hydrofracturing and ice-cliff calving processes incorporated here are observed phenomena, and they are tested under both modern and geological settings.

Both the LIG and Pliocene ensembles saturate at the upper range of ensemble parameter values (Extended Data Figure 1). The LIG is sufficiently warm to cause complete WAIS retreat, but not warm enough to trigger retreat into East Antarctic basins, even if our nominal ice-cliff calving limit of 13,000 m yr^{-1} is doubled (Extended Data Figure 1). Similarly, maximum ice loss in the Pliocene ensemble reflects the loss of almost all marine-based ice as supported by observations[33], but not more. As such, we stress that the geological constraints do not rule out the possibility of faster ice-cliff calving rates than observed on Greenland.

Model projections and implications of the Paris Agreement

We run ensembles of the transient response of the AIS to future greenhouse gas emissions scenarios (Methods) representing global mean warming limits of +1.5 ºC, +2 ºC, and +3 ºC (similar to current policies and Nationally Determined Contributions, NDCs[29]), and extended RCP2.6, RCP4.5, and RCP8.5 scenarios[30]. Only those 109 model parameter combinations validated by IMBIE and geological constraints (Extended Data Figure 4d) are included in the analysis (Fig. 1, Table 1). The +1.5 ºC, +2 ºC, and +3 ºC scenarios assume there is no overshoot in temperature; i.e., once these global mean temperature targets are reached in 2040, 2060, and 2070, respectively, atmosphere and ocean forcings are held constant.

In the +1.5 ºC and +2 ºC ensembles, Antarctic ice loss continues at a pace similar to today throughout the 21st century. The median contribution to sea level in 2100 is 8 cm with +1.5 ºC warming and 9 cm with +2 ºC. In sharp contrast, ~10% of the ensemble members in the +3 ºC scenario show the onset of major WAIS retreat in the second half of the 21st century. This skews the upper bound of the +3 ºC distribution (33 cm at the 90th percentile), substantially increasing the ensemble median (15 cm in 2100) relative to the +1.5 ºC and +2 ºC scenarios (Fig. 1). On late

21^{st} century and longer timescales, the jump in ice loss at +3 ºC is mainly caused by Thwaites Glacier retreat (Fig. 2), which destabilizes the entire WAIS in some ensemble members (Extended Data Figure 5).

In the more extreme RCP8.5 scenario, thinning and hydrofracturing of buttressing ice shelves becomes more widespread, triggering marine ice sheet instabilities in both West and East Antarctica. The RCP8.5 median contribution to GMSL is 34 cm by 2100 (Fig. 1). This is substantially less than reported by ref.[8] (64-105 cm), due to a combination of recalibrated and improved model physics, and revised atmospheric forcing (Methods) that delays the onset of surface melt by ~25 years. Despite the slower onset of surface melt, the median contribution to GMSL reaches 1 m by 2125 and rates exceed 6 cm yr^{-1} by 2150 (Extended Data Figures 6,7). By 2300, Antarctica contributes 9.6 m of GMSL rise under RCP8.5, almost 10 times more than simulations limiting warming to +1.5 ºC.

In alternative ensembles, the upper bound of VCLIFF is reduced from 13 km yr^{-1} to 11 km yr^{-1} or 8 km yr^{-1} to reflect Jakobshavn's recent slowdown[17], but the effect on the calibrated ensemble medians is small (Extended Data Table 2). Ensembles using 13 km yr^{-1} as the upper bound (Fig. 1, Table 1) are preferred (Methods), based on the outcomes of history matching (Extended Data Figure 1,4) and observations at Jakobshavn demonstrating that such rates are indeed possible.

Future simulations without hydrofracturing and ice-cliff calving produce less GMSL rise than our ensemble medians (Extended Data Figure 6). Enhanced precipitation in East Antarctica partially compensates for MISI-driven retreat in West Antarctica, in line with other models that do not include ice-cliff calving[42], but these simulations are excluded from the projections because of their inability to reproduce the Pliocene or LIG.

Negative feedbacks slowing future ice loss

Because our model includes hydrofracturing, the onset of major retreat is sensitive to the pace of future warming in our atmospheric forcing. We compare our RCM/CCSM4-driven RCP8.5 ensemble to two alternative simulations, with atmosphere and ocean forcing supplied by the NCAR CESM 1.2.2 GCM. Both CESM-forced simulations follow RCP8.5, but one includes Antarctic meltwater feedback (Methods), accomplished by adding time-evolving and spatially distributed liquid water and solid ice discharge at the appropriate ocean grid cells in the GCM[43].

Accounting for Antarctic meltwater discharge in CESM expands Southern Ocean sea ice, stratifies the upper ocean, and warms the subsurface (400 m water depth) by 2-4 ºC around most of the Antarctic margin in the early 22^{nd} century[43]. Conversely, the expanded sea ice suppresses surface atmospheric warming by more than 5 ºC, slowing the onset of surface melt and hydrofracturing in the ice sheet model. The net result of competing sub-surface ocean warming (enhanced sub-shelf melt) and atmospheric cooling (reduced surface melt) produces a substantial negative feedback on the pace of ice-sheet retreat (Fig. 1h). This is contrary to the findings of ref.[38] that found a net positive (ocean-driven) meltwater feedback, using an ice-sheet model without hydrofracturing and less sensitive to surface meltwater. The CESM-driven simulations bracket our RCM/CCSM4-driven ensembles, supporting the timing of retreat in our main ensembles. Our RCM and CESM1.2.2 climate forcings are evaluated relative to independent CMIP5 and CMIP6 GCMs in Supplementary Information).

We test two additional negative feedback mechanisms proposed to provide a stabilizing influence on marine ice-sheet retreat. First, the potential for channelized supraglacial runoff of meltwater to delay or stop ice-shelf hydrofracturing[44] is examined by reducing water-enhanced surface crevassing in regions of compressional ice-shelf flow (Supplementary Information). Despite the reduced influence of meltwater we find that hydrofracturing in a warming climate can still occur near ice shelf calving fronts where the ice is thinnest, convergence and buttressing are minimal[4], and air temperatures (melt rates) are highest. Once initiated, meltwater-enhanced calving near the edge of the shelf reduces compressional flow in the ice upstream and the calving propagates. As a result, reduced wet crevassing in compressional flow does little to protect buttressing ice shelves[45] and the impact on our simulations is minimal (Supplementary Figure 3).

Second, we examine the potential for rapid bedrock uplift and ice-ocean gravitational effects to lower relative sea level and reduce ice loss at retreating grounding lines[46]. Exceptionally fast uplift rates due to low mantle viscosities in the Amundsen Sea sector of West Antarctica have been invoked to suggest future retreat of the WAIS might be slowed by this effect more than previously considered[47]. This is tested by replacing the model's standard Elastic Lithosphere/Relaxing Asthenosphere representation of deforming bedrock with a more complete viscoelastic (Maxwell) Earth model, combining radially varying, depth-dependent lithosphere and viscosity structure, and gravitationally self-consistent sea level calculations (Methods)[46]. In simulations assuming the lowest inferred upper mantle viscosity values[47] with rapid bedrock uplift under all of West Antarctica, we find limited potential for uplift and sea-level feedback to slow the pace of retreat over the next ~two centuries (Extended Data Figure 8). This finding is consistent with other recent studies[48,49]; however, we caution that future work should explore these effects at higher resolution and with a full 3-D representation of Earth structure[50] including lateral heterogeneity of viscoelastic properties under both West and East Antarctica.

Implications of delayed mitigation and overshooting 1.5 ºC

An additional set of simulations were run using a single combination of ice model parameters representing calibrated ensemble averages (Extended Data Table 1). The simulations either maintain current (2020) atmosphere and ocean conditions without any future warming, or begin to follow the +3 ºC emissions pathway, except assuming CDR mitigation is initiated at different times in the future beginning in 2030, 2040, 2050, 2060, 2070, 2080, 2090, 2100, 2150, or 2200. We optimistically assume CDR technologies will be capable of reducing CO_2 atmospheric mixing ratios with an e-folding time of one century (Fig. 3a).

We find that without any future warming beyond 2020, Antarctica continues to contribute to 21st century sea level rise at a rate roughly comparable to today, producing 5 cm of GMSL rise by 2100 and 1.34 m by 2500 (Fig. 3; Table 2). In simulations initially following the +3 ºC pathway but with subsequent CDR, we find that delaying CDR until after 2060 allows a sharp jump in the pace of 21st century sea level rise (Fig. 3b). Every decade that CDR mitigation is delayed has a substantial long-term consequence on sea level, despite the fast decline in CO_2 and return to cooler temperatures (Fig. 3c). Once initiated, marine-based Antarctic ice loss is found to be unstoppable on these timescales in all of the mitigation scenarios tested here (Fig. 3). The commitment to sustained ice loss is caused by the warmer (softer) ice sheet, and the onset of marine ice sheet instabilities triggered by the loss of ice shelves that cannot recover in a warmer ocean with a long thermal memory (Fig. 3c).

In sum, these results demonstrate that current policies allowing +3 ºC or more of future warming could exceed a threshold, triggering extensive thinning and loss of vulnerable Antarctic ice shelves and ensuing marine ice sheet instabilities starting within this century. The resulting sea level rise would be irreversible on multi-century timescales, even if atmospheric temperatures were to return to preindustrial-like values (Fig. 3). Relative to +3 ºC, sea level rise resulting from the +1.5 ºC and +2 ºC aspirations of the Paris Agreement (Fig. 1) would have much less impact on low-lying coastlines, islands, and major population centers, pointing to the importance of ambitious mitigation.

Strong circum-Antarctic atmospheric cooling feedback caused by fresh water and ice discharge[43] slows the pace of retreat under RCP8.5 (Fig. 1h). However, other proposed negative feedbacks on ice loss associated with ice-Earth-sea level interactions and reduced hydrofracturing through surface runoff appear to have minimal potential to slow the pace of ice loss on 21st-22nd century timescales.

While we attempt to constrain some parametric uncertainty, this study uses a single ice-sheet model, and structural uncertainty is only accounted for in the model improvements described herein. Similarly, our main ensembles (Fig. 1) use a single method of climate forcing, although the magnitude and pace of future warming in our simulations is comparable to other state-of-the-art climate models (Supplementary Figure 1,2) and alternative simulations driven by CESM1.2.2 produce similar results (Fig. 1h). More work is clearly needed to explore additional model parameters using multiple ice-sheet models that account for processes associated with MISI and MICI, and with alternative boundary conditions and future climate forcing that includes interactive climate-ice sheet coupling.

Ice-cliff calving remains a key wild card. While founded on basic physical principles and observations, its potential to produce even faster rates of ice loss than simulated here remains largely untested with process-based models of mechanical ice failure. Here we find that limiting rates of ice-cliff calving to those observed on Greenland can still drive multi-meter per century rates of sea level rise from Antarctica (Extended Data Figure 7). Given the bedrock geography of the much larger and thicker AIS, the possibility of even faster mechanical ice loss should be a top priority for further investigation.

Table 1 | Antarctic sea level contributions

Scenario	2100	2200	2300
+1.5ºC	0.08 (0.06-0.10)	0.52 (0.22-0.77)	1.03 (0.61-1.22)
+2.0 ºC	0.09 (0.07-0.11)	0.58 (0.26-0.83)	1.09 (0.68-1.25)
+3.0 ºC (NDCs)	0.15 (0.08-0.27)	0.81 (0.45-1.25)	1.54 (1.04-2.03)
RCP2.6	0.09 (0.07-0.12)	0.58 (0.27-0.85)	1.10 (0.71-1.36)
RCP4.5	0.09 (0.07-0.12)	0.67 (0.35-0.91)	1.29 (0.90-1.59)
RCP8.5	0.34 (0.20-0.53)	5.33 (3.70-7.64)	9.57 (6.87-13.55)

Ensemble medians using IMBIE, Last Interglacial, and Pliocene observational constraints reported in meters relative to 2000. Values in parentheses are the 17^{th}-83^{rd} percentiles (likely range). Scenarios refer to the maximum global mean temperature reached relative to pre-industrial (1850) or following extended RCPs. Alternative ensemble outcomes using more restrictive ranges of ice-cliff calving parameters are provided in Extended Data Table 2.

Table 2 | Long-term Antarctic sea level contributions with delayed CDR

CDR scenario	2100	2300	2500
+3 ºC scenario, no CDR	0.21	1.77	2.63
CDR in 2200	0.21	1.70	2.39
CDR in 2150	0.21	1.58	2.29
CDR in 2100	0.21	1.34	2.04
CDR in 2090	0.21	1.33	2.04
CRD in 2080	0.20	1.30	2.03
CDR in 2070	0.17	1.25	1.99
CDR in 2060	0.08	1.09	1.77
CDR in 2050	0.07	1.06	1.71
CDR in 2040	0.06	0.94	1.59
CDR in 2030	0.05	0.76	1.43
2020 constant forcing	0.05	0.75	1.34

Ice sheet simulations corresponding to Figure 3, using average calibrated hydrofracturing and ice-cliff calving parameter values (Extended Data Table 1). Values are reported in meters relative to 2000. The simulations follow the standard +3 ºC (NDC) emissions scenario or with carbon dioxide reduction (CDR) beginning in 2200, 2150, 2100, 2090, 2080, 2070, 2060, 2050, or 2030. An alternative scenario maintains the atmosphere and ocean climate forcing at 2020 (with no additional future warming).

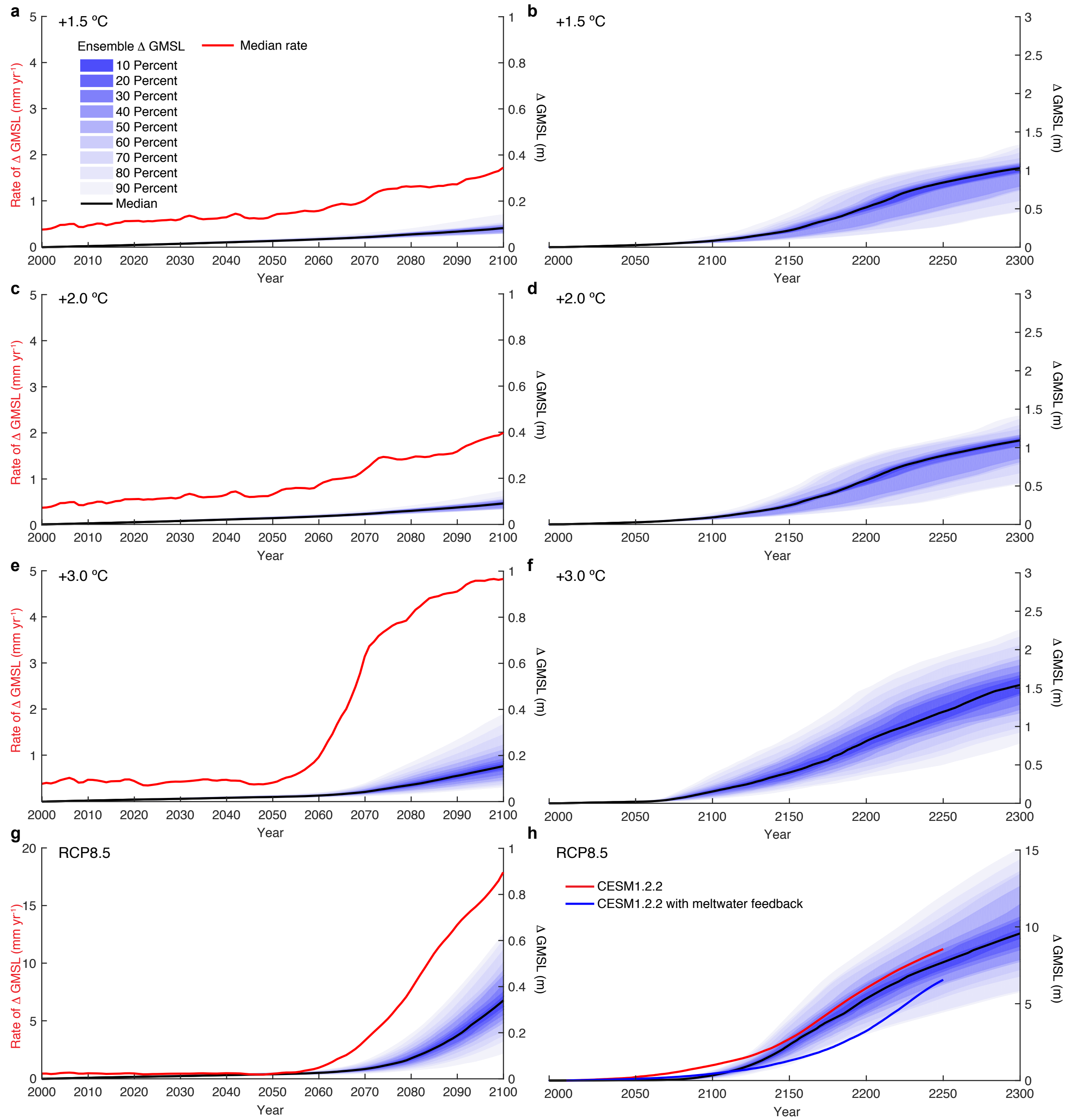

Figure 1 | Antarctic contribution to GMSL rise under a range of emissions scenarios. The fan charts show the time-evolving uncertainty and range around the median ensemble value (black line) in 10% increments. Panels in the left column show ensemble results from 2000 to 2100 including median rates of GMSL rise (red line). The right column is extended to 2300. **a**, **b**, Emissions consistent with a +1.5 ºC global mean warming scenario. **c**, **d**, Emissions consistent with +2.0 ºC, **e**, **f**, Emissions consistent with +3.0 ºC. **g**, **h**, RCP8.5. **h**, Two additional RCP8.5 simulations are shown with average calibrated parameter values associated with wet crevassing/hydrofracturing (CALVLIQ=107 m^{-1} yr^{2}) and ice-cliff calving (VCLIFF=7.7 km yr^{-1}), but with atmosphere and ocean forcing provided by the NCAR CESM1.2.2 GCM with (blue line) and without (red line) Antarctic meltwater feedback[43]. Note the expanded y-axes in **g** and **h.**

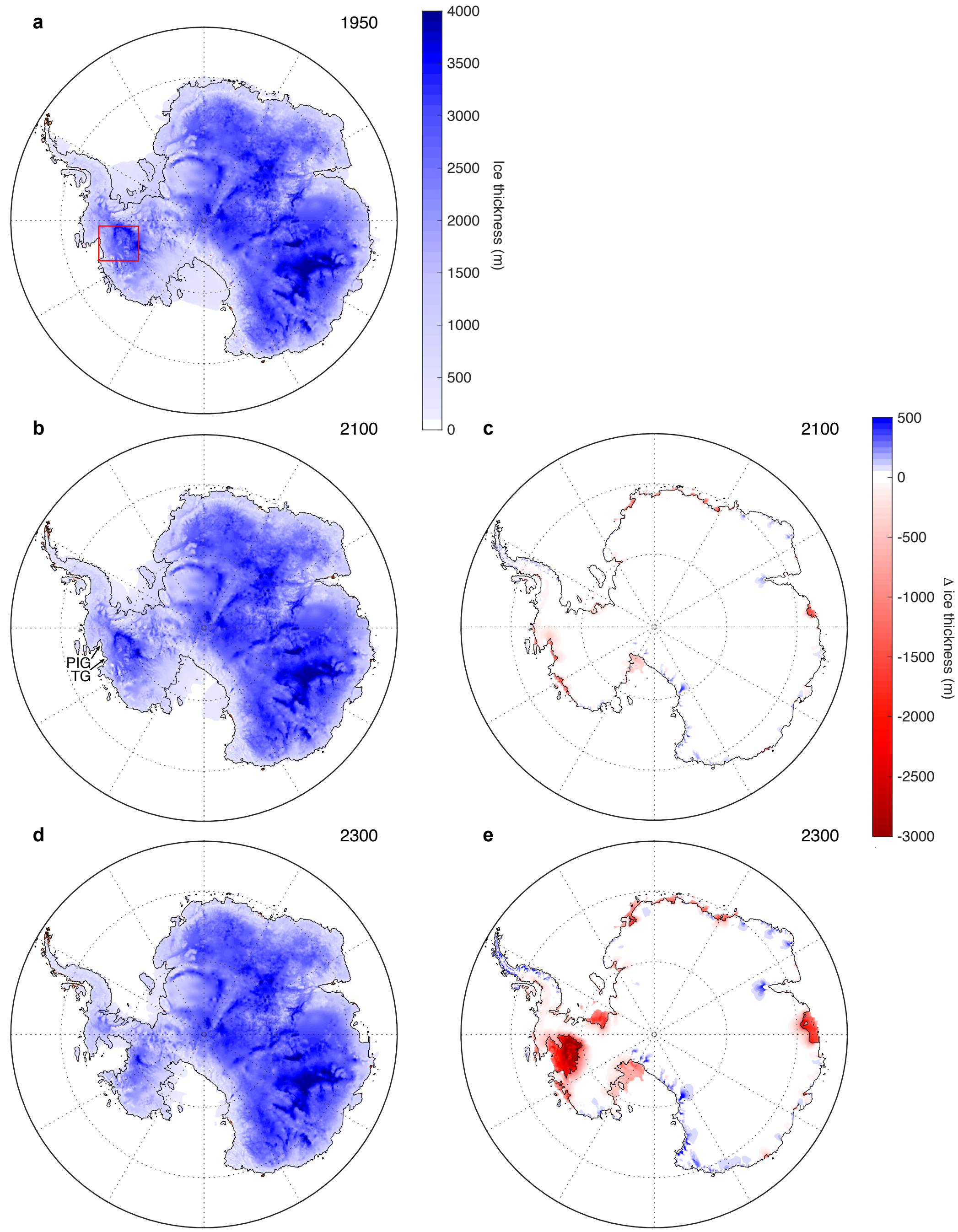

Figure 2 | Ice sheet evolution following a +3 ºC global warming emissions trajectory. A single +3 ºC ensemble member with average hydrofracturing and ice-cliff calving parameters. Transient atmosphere and ocean forcing follows the +3 ºC scenario, roughly consistent with current policies (NDCs). Floating and grounded ice thickness is shown in blue. The grounding line position is shown with a black line. The red square over the Thwaites Glacier (TG) and Pine Island Glacier (PIG) sector of West Antarctica corresponds to the high resolution (1,000 m) nested model domain in Extended Data Figure 5. **a**, Ice sheet initial conditions. **b**, The model ice sheet in 2100, showing the onset of major retreat of Thwaites Glacier. **c**, Change in ice thickness in 2100, **d**, The ice sheet in 2300 with Thwaites Glacier retreat leading to the loss of the WAIS. **e**, Change in ice thickness in 2300.

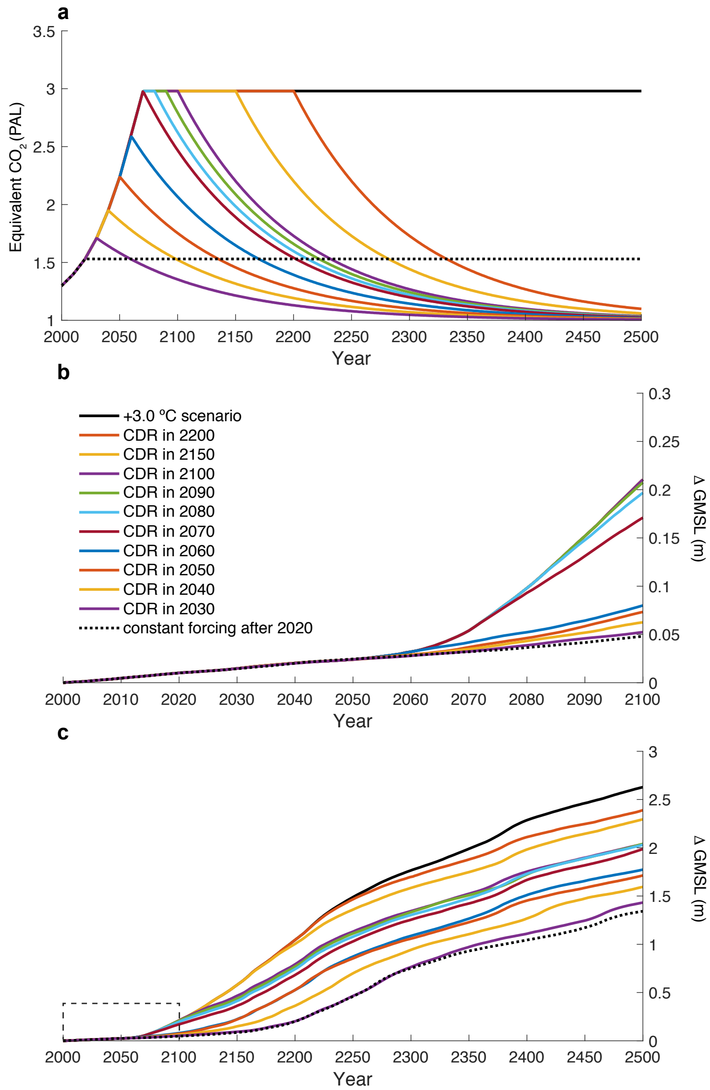

Figure 3 | Ice sheet thresholds and commitments to sea-level rise from Antarctica with delayed greenhouse gas mitigation. **a**, Greenhouse gas (GHG) emissions scenarios initially following the +3 ºC (NDCs) scenario, followed by CDR (carbon dioxide reduction/negative emissions), optimistically assuming relaxation toward preindustrial levels with an e-folding time of 100 years. The timing when CDR commences is shown in **b**. The solid black line is the same +3 ºC simulation shown in Fig. 2 and Extended Data Figure 5. The dashed black line assumes there is no additional GHG increase or warming after 2020. GHG concentrations are shown in CO_2-equivalent, in units of preindustrial atmospheric level (PAL, 280 ppm). **b**, GMSL contributions from Antarctica, corresponding to the scenarios in **a**, over the 21st century. All simulations use identical model physics and average hydrofracturing and ice-cliff calving parameters. Note the sharp increase in late 21st-century ice loss when CDR is delayed until 2070. **c**, The same as **b**, but extended to 2500. Note the large differences in the commitment to long-term GMSL rise, depending on the timing when mitigation begins. All scenarios exceed 1 m by 2500 and no scenarios show recovery of the ice sheet, including those returning to near-preindustrial levels of GHGs by ~2300.

References

1 Shepherd, A. *et al.* Mass balance of the Antarctic Ice Sheet from 1992 to 2017. *Nature* **558**, 219-222 (2018).

2 Shepherd, A. *et al.* Mass balance of the Greenland Ice Sheet from 1992 to 2018. *Nature* **579**, 233-239 (2020).

3 Morlighem, M. *et al.* Deep glacial troughs and stabilizing ridges unveiled beneath the margins of the Antarctic Ice Sheet. *Nature Geoscience* **13**, 132-137 (2020).

4 Fürst, J. J. *et al.* The safety band of Antarctic ice shelves. *Nature Climate Change* **6**, 479 (2016).

5 Weertman, J. Stability of the junction of an ice sheet and an ice shelf. *Journal of Glaciology* **13**, 3-11 (1974).

6 Schoof, C. Ice sheet grounding line dynamics: Steady states, stability, and hysteresis. *Journal of Geophysical Research-Earth Surface* **112**, F03S28 (2007).

7 Pollard, D., DeConto, R. M. & Alley, R. B. Potential Antarctic ice sheet retreat driven by hydrofracturing and ice cliff failure. *Earth and Planetary Science Letters* **412**, 112-121 (2015).

8 DeConto, R. M. & Pollard, D. Contribution of Antarctica to past and future sea-level rise. *Nature* **531**, 591-597 (2016).

9 Paolo, F. S., Fricker, H. & Padman, L. Volume loss from Antarctic ice shelves is accelerating. *Science Express* (2015).

10 Gudmundsson, G. H. Ice-shelf buttressing and the stability of marine ice sheets. *The Cryosphere* **7**, 647-655 (2013).

11 Bassis, J. N. & Walker, C. C. Upper and lower limits on the stability of calving glaciers from the yield strength envelope of ice. *Proceedings of the Royal Society A* **468**, 913-931 (2012).

12 Parizek, B. R. *et al.* Ice-cliff failure via retrogressive slumping. *Geology* **47**, 1-4 (2019).

13 Clerc, F., Minchew, B. M. & Behn, M. D. Marine ice cliff instability mitigated by slow removal of ice shelves. *Geophysical Research Letters* **46**, 2019GL084183 (2019).

14 Vaughan, D. G. Relating the occurrence of crevasses to surface strain rates. *Journal of Glaciology* **39**, 255-266 (1993).

15 Schlemm, T. & Levermann, A. A simple stress-based cliff-calving law. *The Cryosphere* **13**, 2475-2488 (2019).

16 An, L. *et al.* Bed elevation of Jakobshavn Isbræ, West Greenland, from high-resolution airborne gravity and other data. *Geophysical Research Letters* **44**, 3728-3736 (2017).

17 Khazendar, A. *et al.* Interruption of two decades of Jakobshavn Isbrae acceleration and thinning as regional ocean cools. *Nature Geoscience* **12**, 277-283 (2019).

18 Parizek, B. R. *et al.* Ice-cliff failure via retrogressive slumping. *Geology* **47**, 449-452 (2019).

19 Joughin, I. *et al.* Seasonal to decadal scale variations in the surface velocity of Jakobshavn Isbrae, Greenland: Observation and model-based analysis. *Journal of Geophysical Research-Earth Surface* **117** (2012).

20 Rignot, E. *et al.* Accelerated ice discharge from the Antarctic Peninsula following the collapse of larsen b ice shelf. *Geophysical Research Letters* **31**, L18401 (2004).

21 Scambos, T. A., Berthier, E. & Shuman, C. A. The triggering of subglacial lake drainage during rapid glacier drawdown: Crane Glacier, Antarctic Peninsula. *Annals of Glaciology* **52**, 74-82 (2011).

22 Milillo, P. *et al.* Heterogeneous retreat and ice melt of thwaites glacier, West Antarctica. **5**, eaau3433 (2019).

23 Atkinson, B. K. Subcritical crack growth in geological materials. *Journal of Geophysical Research: Solid Earth* **89**, 4077-4114 (1984).

24 Kuipers Munneke, P., Ligtenberg, S. R. M., van den Broeke, M. R. & Vaughan, D. G. Firn air depletion as a precursor of Antarctic ice-shelf collapse. *Journal of Glaciology* **60**, 205-214 (2014).

25 Banwell, A. F., Willis, I. C., Macdonald, G. J., Goodsell, B. & MacAyeal, D. R. Direct measurements of ice-shelf flexure caused by surface meltwater ponding and drainage. *Nature Communications* **10**, 730 (2019).

26 Trusel, L. D. *et al.* Divergent trajectories of Antarctic surface melt under two twenty-first-century climate scenarios. *Nature Geoscience* **8**, 927-932 (2015).

27 Robel, A. A. & Banwell, A. F. A speed limit on ice shelf collapse through hydrofracture. *Geophysical Research Letters* **46**, 12092-12100 (2019).

28 Rhodes, C. J. The 2015 paris climate change conference: Cop21. *Science Progress* **99**, 97-104 (2016).

29 Fawcett, A. A. *et al.* Can Paris pledges avert severe climate change? *Science* **350**, 1168-1169 (2015).

30 van Vuuren, D. P. *et al.* The representative concentration pathways: An overview. *Climatic Change* **109**, 5-31 (2011).

31 Edwards, T. L. *et al.* Revisiting Antarctic ice loss due to marine ice-cliff instability. *Nature* **566**, 58-64 (2019).

32 Dutton, A., Webster, J. M., Zwartz, D. & Lambeck, K. Tropical tales of polar ice: Evidence of last interglacial polar ice sheet retreat recorded by fossil reefs of the granitic seychelles islands. *Quaternary Science Reviews* **107**, 182-196 (2015).

33 Grant, G. R. *et al.* The amplitude and origin of sea-level variability during the pliocene epoch. *Nature* **574**, 237-241 (2019).

34 Dumitru, O. A. *et al.* Constraints on global mean sea level during pliocene warmth. *Nature* **574**, 233-236 (2019).

35 Velicogna, I., Sutterley, T. C. & van den Broeke, M. Spatially varying ice mass acceleration of the polar ice sheets from grace. *Geophysical Research Letters* **41**, 9130-8137 (2014).

36 Rohling, E. J. *et al.* Asynchronous Antarctic and Greenland ice-volume contributions to the last interglacial sea-level highstand. *Nature Communications* **10**, 5040 (2019).

37 Cook, C. P. *et al.* Dynamic behaviour of the east Antarctic ice sheet during pliocene warmth. *Nature Geoscience* **6**, 765-769 (2013).

38 Golledge, N. R. *et al.* Global environmental consequences of twenty-first-century ice-sheet melt. *Nature* **566**, 65-72 (2019).

39 Seroussi, H. & Morlighem, M. Representation of basal melting at the grounding line in ice flow models. *The Cryosphere* **12**, 3085-3096 (2018).

40 Tsai, V. C., Stewart, A. L. & Thompson, A. F. Marine ice-sheet profiles and stability under coulomb basal conditions. *Journal of Glaciology* **61**, 205-215 (2017).

41 Pattyn, F. *Sea-level response to melting of Antarctic ice shelves on multi-centennial time scales with the fast elementary thermomechanical ice sheet model (f.Etish v1.0)*. (2017).
42 Seroussi, H. *et al.* Ismip6 Antarctica: A multi-model ensemble of the Antarctic ice sheet evolution over the 21st century. *The Cryosphere Discuss.* **2020**, 1-54 (2020).
43 Sadai, S., Condron, A., DeConto, R. & Pollard, D. Future climate response to Antarctic ice sheet melt caused by anthropogenic warming. *Science Advances* **6**, eaaz1169 (2020).
44 Bell, R. E. *et al.* Antarctic ice shelf potentially stabilized by export of meltwater in surface river. *Nature* **544**, 344-348 (2017).
45 Lai, C.-Y. *et al.* Vulnerability of Antarctica's ice shelves to meltwater-driven fracture. *Nature* **584**, 574-578 (2020).
46 Gomez, N., Pollard, D. & Holland, D. Sea level feedback lowers projections of future Antarctic ice sheet mass loss. *Nature Communications* **6** (2015).
47 Barletta, V. R. *et al.* Observed rapid bedrock uplift in amundsen sea embayment promotes ice-sheet stability. *Science* **360**, 1335-1339 (2018).
48 Pollard, D., Gomez, N. & DeConto, R. Variations of the Antarctic ice sheet in a coupled ice sheet-earth-sea level model: Sensitivity to viscoelastic earth properties. *Journal of Geophysical Reseach-Earth Surface* **122**, 2169-9011 (2017).
49 Larour, E. *et al.* Slowdown in Antarctic mass loss from solid earth and sea-level feedbacks. *Science*, eaav7908 (2019).
50 Powell, E., Gomez, N., Hay, C., Latychev, K. & Mitrovica, J. X. Viscous effects in the solid earth response to modern Antarctic ice mass flux: Implications for geodetic studies of wais stability in a warming world. *Journal of Climate* **33**, 443-459 (2020).

Methods

Ice sheet modeling framework. The ice sheet-shelf model uses hybrid ice dynamics[51] with an internal boundary condition on ice velocity at the grounding line[6]. Grounding lines can migrate freely and the model accounts for the buttressing effects of ice shelves with pinning points and side shear (see Supplementary Information). In our solution of the dynamical shallow shelf (SSA) equations, ice velocities across grounding lines are imposed as a function of local sub-grid ice thickness, accurate to the limit of the resolved bathymetry. This is also true for diagnosed stresses and ice-cliff failure rates which makes the model largely independent of grid resolution (Extended Data Figure 5). A resolution of 10 km is used for continental simulations used in our main ensembles (Fig. 1-3). A nested 1-km grid is used for a select simulation over West Antarctica (Extended Data Figure 5). The model uses a standard Weertman-type basal sliding law[51], with basal sliding coefficients determined by an inverse method iteratively matching model ice-surface elevations to observations under modern climate conditions[52]. We use Bedmap2[53] bathymetric boundary conditions. Using alternative BedMachine[3] bathymetry is found to have only a small effect on continental-scale sea-level projections (<1.5% difference under RCP8.5 in 2300). Several advances relative to previous versions of the model[7,8,51] are described below and in Supplementary Information.

Sub-ice melt rates. The model used here includes an updated treatment of sub-ice oceanic melting. Oceanic melt rates (OM) are calculated at each floating ice grid cell as a quadratic function of the difference between nearest sub-surface ocean temperatures at 400-m water depth, and the pressure-melting point of ice[51,54]. The model accounts for evolving connectivity between a given ice model grid cell and the open ocean, and elevated plume melt on subsurface vertical ice faces[51]. All melt calculations are performed with spatially uniform physics, including a single, uniform coefficient in the ocean melt relation based on a 625-member ensemble of simulations of WAIS retreat through the last deglaciation[55]. Although it would be possible to invert for a distribution of coefficients within each basin based on modern ice-shelf melt observations[38], their patterns are likely to change substantially within the time scales of our simulations as ocean circulation, grounding-line extents, and cavity geometries evolve. A 1.5 ºC sub-surface ocean temperature adjustment is used in the Amundsen Sea sector to bring ocean melt rates closer to observations[56] when using CCSM4 ocean-model temperatures that underestimate observed shelf bottom water temperatures[57]. This is a substantial improvement relative to the 3 ºC temperature adjustment required previously[8].

Ice shelf hydrofracturing. In the model, surface crevasses deepen as a function of the stress field and local meltwater and rainfall availability[7,8,58], leading to hydrofracturing when surface and basal crevasses penetrate 75% or more of the total ice thickness. With greatly increased surface melt, model ice shelves can be completely lost. In the standard wet crevassing scheme, we assume a quadratic relationship between surface crevasse penetration depth d_w (m) and total meltwater production R (rain plus surface melt minus refreezing, m yr^{-1}). A tunable prefactor CALVLIQ is varied between zero (no meltwater influence on crevassing) and 195 m^{-1} yr^{2} in the ensembles presented in the main text.

$$d_w = CALVLIQ\ R^2$$

Calving occurs in places where the sum of surface and basal crevasse penetration caused by extensional stresses, accumulated strain (damage), thinning, and meltwater (d_w), exceeds the critical fraction (0.75) of total ice thickness (see appendix B of ref.[7]).

The crevassing scheme is modified here relative to previous model versions[7,8,51], by reducing wet crevassing in areas of low-to-moderate meltwater production (<1500 mm yr^{-1}), ramping linearly from zero where no meltwater is present, to d_w where R =1500 mm yr^{-1}. This small modification improves performance by maintaining more realistic ice shelf calving fronts under present climate conditions, although it conservatively precludes the loss of ice shelves with thicknesses comparable to the Larsen B until R approaches ~1400 mm yr^{-1}, which is more than observed prior to the actual collapse (~750 mm yr^{-1})[3]. While embedded liquid water in firn and partial refreezing of meltwater is accounted for[8,59], the detailed evolution of firn density and development of internal ice lenses are not, which could impact the timing when hydrodrofacturing is simulated to begin. A modification to hydrofracturing described in

Supplementary Information tests the possible influence of channelized meltwater flow and supraglacial runoff in compressional ice shelf regimes.

Calving and ice-cliff failure. Two modes of brittle fracturing causing ice loss are represented in the model: 1) "standard" calving of ice bergs from floating ice, and 2) structural failure of tall ice cliffs at the grounding line. Similar to other models, standard calving depends mainly on the grid-scale divergence of ice flow, producing crevasses to depths at which the extensional stress is equal to the hydrostatic imbalance[58]. Crevasse penetration is further increased as a function of surface meltwater and rain availability (see above).

Unlike most continental-scale models we also account for ice-cliff calving at thick, marine-terminating grounding lines. Such calving is a complex product of forces related to glacier speed, thickness, longitudinal stress gradients, bed conditions, side shear, preexisting crevasses, mélange, and other factors[60]. Determining the precise mode and rate of failure is the focus of ongoing work[12,13,15,61], but to date, a suitable physically based calving model has yet to be developed. In our model[7,8], ice-cliff calving occurs where static stresses at the calving front (assumed to be exactly at floatation) begin to exceed the depth-averaged yield strength of glacial ice, assumed here to be 0.5 MPa[11]. We account for crevassing near the cliff face (influenced by the stress regime and the presence of meltwater[7]) which thins the supportive ice column and increases the stress at the ice front. Where the critical stress threshold is exceeded, ice-cliff calving is applied as a horizontal wastage rate, ramping linearly from zero up to a maximum rate as effective cliff heights (adjusted for buttressing and crevassing) increase from 80 to 100 m and above. This maximum calving rate is treated as a tunable model parameter (VCLIFF), replacing the arbitrary default value of 3 km yr^{-1} in equation (A.4) of ref.[7]. In this formulation, ice-cliff calving rates in places diagnosed to be undergoing structural failure are generally much smaller than VCLIFF (Extended Data Figure 5). We note that the linear cliff height-calving relationship with an imposed calving limit (VCLIFF) used here is conservative relative to another proposed calving law[15] assuming a power law dependence on cliff height and no upper bound on the calving rate. Furthermore, our model numerics preclude regular calving in places undergoing ice-cliff failure, so the computed ice-cliff calving rate can be considered the sum of all calving processes at thick marine-terminating ice fronts. This allows direct comparison of model calving (Extended Data Figure 5) with observations. Mélange can slow calving by providing some back stress at confined calving fronts[62,63], but it has limited effect on the large unconfined widths of Antarctic outlets[64], so it is ignored here.

Ensemble parameters. Our primary perturbed physics ensembles use a 14×14 matrix (n=196) of CREVLIQ and VCLIF in the hydrofracturing and ice-cliff calving parameterizations described above (Extended Data Table 1). The 14 values of CREVLIQ vary between 0 and 195 m^{-1} yr^{2} in evenly spaced increments. VCLIFF varies between 0 and 13 km yr^{-1}. Previous studies[7,8] considered a smaller, arbitrary range of VCLIFF values up to 5 km yr^{-1}, however observed rates of horizontal ice loss through ice-cliff calving can reach 13 km yr^{-1} at the terminus of Jakobshavn Isbræ in West Greenland[16], so we limit the top of our parameter range in our main ensembles to this observationally justifiable value. As discussed in the main text, this upper bound might be too small for Antarctic settings with thicker ice margins, taller unconfined ice fronts, and higher deviatoric stresses at unbuttressed grounding lines. Select simulations extending the upper bounds of CALVLIQ and VCLIFF above 195 m^{-1} yr^{2} and 13 km yr^{-1}, respectively, are shown in Extended Data Figure 1. Setting these parameter values to zero (Extended Data Figures 1,6) effectively eliminates hydrofracturing and ice-cliff calving, limiting rates of ice loss to processes associated with standard calving, surface mass balance, sub-ice melt, and MISI as in most other continental-scale ice sheet models.

Ensemble scoring based on recent observations. Future ice sheet simulations begin in 1950 to allow comparisons with observations over the satellite era. For consistency, ice sheet initial conditions (ice thickness, bed elevation, velocity, basal sliding coefficients, and internal ice and bed temperatures) follow the same procedure as ref.[8] and are identical in all simulations. Initialization involves a 100,000-kyr spinup using observed mean annual ocean climatology[65] and standard SeaRISE[66] atmospheric temperature and precipitation fields[67].

We consider three different estimates of recent changes in Antarctic ice mass to test the performance of each ensemble member with a unique combination of model physical parameters (Extended Data Table 1). We use the average annual mass change $\frac{d\bar{M}}{dt}$ from 1992-2017 (equivalent to a GMSL change of 0.15-0.46 mm yr^{-1}) provided by the IMBIE assessment[1] and based on a combination of satellite altimetry, gravimetry, and surface mass balance estimates. We use the 25-year average to minimize the influence of simulated and observed interannual variability (Extended Date Figure 1a) on ensemble scoring, although decadal and longer variability[68] is not fully captured. Alternative target ranges use mass change calculations based solely on the Gravity Recovery and Climate Experiment (GRACE) following the methodology in ref.[35] and updated from April 2002 to June 2017. The glacial isostatic adjustment (GIA) component of the GRACE estimates represents the largest source of uncertainty. We use three GIA models[69-71]. For each model we use a range of GIA corrections generated by the authors using a range of viscosities and lithospheric thicknesses[69-71]. The lower bound of our mass change estimates is calculated using the minimum GIA correction from the three models[69-71] and the upper bound is calculated using the maximum GIA correction. This yields a 2002-2017 average estimate of 0.2-0.54 mm yr^{-1}, close to the central estimate from IMBIE over the same interval. Alternatively, we consider viscosity profiles from each of these studies reported to provide the best fit with observations[69-71]. This substantially narrows and shifts the 2002-2017 range toward higher values (0.39 to 0.53 mm yr^{-1}), which is impactful on our ensemble scoring and future projections, highlighting the need for more precise modern observations. While the uncertainty range of estimates based solely on GRACE is smaller, the longer IMBIE record is used as our default training constraint over the modern era.

Last Interglacial ensemble. Last Interglacial simulations use model physics, parameter values, and initial conditions identical to those used in our Pliocene and future simulations. The ice-driving atmospheric and oceanic climatology representing conditions between 130 and 125 kyr ago is the same as that used in ref.[8], and is based on a combination of regional atmospheric modeling and proxy-based reconstructions of air and ocean temperatures[72]. Differences in the timing and magnitude of our modeled Antarctic ice sheet retreat relative to independent LIG simulations[73] reflect the different approaches to LIG climate forcing and structural differences in our ice sheet models, including the inclusion of hydrofracturing and ice-cliff calving in this study.

Our ensemble scoring uses a Last Interglacial (LIG) target range of Antarctic ice loss equivalent to (3.1-6.1 m), assumed to have occurred early in the interglacial between 129 and 128 kyr ago (Extended Data Figure 1). The range used here is based on a prior estimate of GMSL of 5.9 ± 1.7 m by 128.6 ± 0.8 ka[32] (2σ uncertainty) rounded to the nearest half meter (4.5-7.5 m) to reflect ongoing uncertainty in the magnitude (due to GIA effects and dynamic topography) and timing of LIG sea level estimates[32,74]. The Antarctic component is deconvolved from the GMSL value by assuming Greenland contributed no more than 1 m before 128 ka[75-77], with an additional 0.4 m contributed by thermosteric effects[75]. Contributions from mountain glaciers in the early LIG are not known are not included in our simple accounting. We find that rounding the exact GMSL values in ref.[32] (5.9 ± 1.7 m or 2.8-6.2 m after accounting for Greenland and thermosteric components) has no appreciable effect on the outcome of the calibrated ensembles. The target range of 3.1-6.1 m used here is lower than the 3.6-7.4 m range used in ref.[8], but we emphasize that it is based on a coral record from a single location (Seychelles) and ongoing work may further refine this range. For example, a recent study[73] attempting to simultaneously fit relative sea level data at several locations is able to reproduce early LIG changes observed in the Seychelles without a substantial contribution from Antarctica, but it requires a thin lithosphere in the earth model used to correct for GIA. Conversely, another study[78] indicates that a North American ice sheet may have persisted until ~126 ka or later. If true, this would require a substantial Antarctic contribution to GMSL to offset remaining North American ice in the early LIG. These alternative scenarios remain speculative but they highlight the ongoing uncertainty in the paleo sea level records. Our LIG and Pliocene ensemble data are provided (Supplementary Data) to allow others to test the impact of alternative paleo sea level interpretations on the future projections.

Pliocene ensemble. Mid-Pliocene simulations also use consistent ice model physics and the same RCM climate forcing described in ref.[8], assuming 400 ppm CO_2, an extreme warm austral summer orbit, and 2 ºC of ocean warming to represent maximum mid-Pliocene warmth in

Antarctica. The ice sheet simulations are run for 5000 model years, the approximate duration that the warm orbital parameters are valid (Extended Data Figure 1). The Pliocene maximum GMSL target range of 11-21 m is based on two recent, independent estimates of warm mid-Pliocene (3.26-3.03 Ma) sea level[33,34]. In ref.[33], shallow-marine sediments are used to estimate the glacial-interglacial range of GMSL variability over this interval. Assuming ± 5 meters of uncertainty in the sea level reconstructions and up to five meters of GMSL change contributed by Greenland, at times orbitally out of phase with the timing of Antarctic ice loss[33], the central estimate of Antarctica's contribution to GMSL is (17.8 ± 5 m). This value is adjusted downward to 16 m, based on an independent estimate derived from Mediterranean cave deposits corrected for geodynamical processes[34]. Combining the lower central estimate of ref.[34] and uncertainty range of ref.[33] provides an Antarctic GMSL target of range of 11-21 m, close to the range of 10-20 m used in ref.[8], albeit with considerable uncertainty.

Future ensembles. We improve on previous work[8] with new atmospheric climatologies used to run future ice-sheet simulations using dynamically downscaled meteorological fields of temperature and precipitation provided by a regional atmospheric model (RCM)[79] adapted to Antarctica. RCM snapshots are run at 1950 and with increasing levels of effective CO_2 (2×, 4×, and 8× preindustrial), while accounting for topographic changes in the underlying ice sheet as described in ref.[8]. The resulting meteorological fields are then time-interpolated and log-weighted to match transient CO_2 concentrations following the emissions scenarios simulated here. This technique is computationally efficient and flexible, allowing a number of multi-century emissions scenarios to be explored, including non-standard RCP scenarios (Fig. 1) and those including CDR mitigation (Fig. 3). Unlike ref.[8], sea-surface temperatures and sea ice boundary conditions in the nested RCM come from the same transient NCAR CCSM4[80] runs that provide the time-evolving sub-surface ocean temperatures used in our sub-ice melt rates calculations. This eliminates the need for an imposed lag between transient greenhouse gas concentrations and equilibrated RCM climates as done previously[8]. Our revised approach delays the future timing when surface meltwater begins to appear on ice-shelf surfaces, and the resulting atmospheric temperatures compare favorably with independent CMIP5 and CMIP6 GCMs (Supplementary Figure 1,2) and NCAR CESM1.2.2 (Fig. 1h.).

Monthly mean surface air temperatures and precipitation from the RCM are used to calculate net annual surface mass balance on the ice sheet. These fields are bilinearly interpolated to the relatively fine ice sheet grid, and temperatures are adjusted for the vertical difference between RCM and ice sheet elevations using a simple lapse-rate correction. The lapse-rate correction is also applied to precipitation based on a Clausius-Clapeyron-like relation. A two-step zero-dimensional box model using positive degree days for snow and ice melt captures the basic physical processes of refreezing vs. runoff in the snow-firn column[8,59]. Total surface melt available to influence surface crevassing (Supplementary Figure 1) is the fraction of meltwater not refrozen in the near-surface, plus any rainwater.

A spatially dependent bias correction based on reanalysis (Supplementary Figure 2) could be applied to the RCM forcing, but such corrections are unlikely to remain stationary. Instead, we apply a uniform 2.9 ºC temperature correction, reflecting the austral summer cold bias in the RCM over ice surface elevations lower than 200 m, where surface melt is most likely to begin. The cold bias, caused by an underestimate of net longwave radiation, is observed in other

Antarctic RCMs and GCMs[81,82]. Correcting for the cold bias and accounting for rainwater increases the total available surface meltwater in our RCP8.5 simulations relative to other studies[26] (see Supplementary Information).

The +1.5 ºC simulations initially follow a RCP4.5 emission trajectory[83], with time-evolving atmospheric fields provided by the RCM and matching sub-surface ocean temperatures from an RCP4.5 CCSM4 simulation[80]. The ice-driving climatology evolves freely until 2040, when global mean surface air temperatures first reach +1.5 ºC relative to 1850. Once the +1.5 ºC temperature target is reached, the atmosphere and ocean forcings are fixed (maintained) at their 2040 levels for the duration of the simulations. The +2 ºC scenario is also based on RCP4.5, but warming is allowed to evolve until 2060. Our +3 ºC ensemble (roughly representing the NDCs) initially follows an RCP8.5 emissions trajectory, with the atmospheric and oceanic forcing fixed beyond 2070, when +3 ºC of global warming is first reached. RCP8.5 is used for the +3 ºC scenario, because 21st century warming does not reach +3 ºC in RCP4.5. 21st century warming trajectories over major Antarctic ice shelves are shown in Supplementary Figure 2. Ice sheet ensembles following standard RCP2.6, RCP4.5, and RCP8.5 scenarios[83] are shown in Extended Data Figure 7 for comparison with ref.[8].

Alternative future ensembles (Extended Data Table 2) truncate the upper bound of the VCLIFF calving parameter from 13 km yr^{-1} (Table 1) to either 11 km yr^{-1} or 8 km yr^{-1}, to account for the possibility that 13 km yr^{-1} calving rates observed at Jakobshavn between 2002 and 2015[16] are not representative of the glacier's long-term behaviour. This reduces the raw ensembles from n=196 to n=168 and n=126, respectively. An upper bound of 8 km yr^{-1} is difficult to justify because higher values can't be excluded by the modern, LIG, and Pliocene history matching. Furthermore, 8 km yr^{-1} is very close to the validated average value of 7.7 km yr^{-1} in the main ensemble. Using an upper bound of 11 km yr^{-1} instead of 13 km yr^{-1} has only a small effect on future projections (Extended Data Table 2). We consider 13 km yr^{-1} a reasonable upper bound for our main ensembles (Fig. 1) because this rate has been observed in nature[16] and because ensemble members using this value cannot be excluded based on model performance (Extended Data Figure 1).

Coupled ice-Earth-sea level model. Most simulations use a standard Elastic Lithosphere/Relaxed Asthenosphere (ELRA) representation of vertical bedrock motion[51]. The ELRA model accounts for time-evolving bedrock deformation under changing ice loads, assuming an elastic lithospheric plate above local isostatic relaxation. Alternative simulations (Extended Data Figure 8) account for full Earth-ice coupling using a viscoelastic (Maxwell) Earth model, combining radially varying, depth-dependent lithosphere and mantle structure, and gravitationally self-consistent sea level calculations following the methodology described in ref.[46].

Seismic[84,85] and geodetic[86,87] observations suggest substantial lateral variability in viscoelastic Earth structure, with lower-than-average viscosities in parts of West Antarctica leading to faster uplift where ice mass is lost at the grounding line. Due to ongoing uncertainties in Earth viscoelastic properties, we test a broad range of viscosity profiles. These include two end-member profiles described in refs.[46,48]; one with a relatively high viscosity profile (HV) consistent with standard, globally tuned profiles and one with a thinned lithosphere and a low viscosity zone of 1019 Pa s in the uppermost upper mantle (LVZ) that is broadly representative of West Antarctica. Here, we test a new profile (BLVZ) similar to LVZ, but assuming a vertical profile with the upper zone one order of magnitude less viscous than in LVZ as recently proposed for the Amundsen Sea region[47]. The BLVZ model is consistent with the best fitting radial Earth model in ref.[47], and uses a lithospheric thickness of 60 km, a shallow upper mantle from 60 km to 200 km depth with a viscosity of 3.98×10^{18} Pa s, a deep upper mantle from 200 km to 400 km with a viscosity of 1.59×10^{19} Pa s, a transition zone from 400 km to 670 km depth with a viscosity of 2.51×10^{19} Pa s, and a lower mantle viscosity of 1×10^{19} Pa s.

Two sets of coupled ice-Earth-sea level simulations are run for each viscosity profile, with and without hydrofracturing and ice-cliff calving enabled (Extended Data Figure 8). Simulations with the brittle processes enabled use values of CALVLIQ (105 m^{-1} yr^{2}) and VCLIFF (6 km yr^{-1}) close to the ensemble averages. The simulations follow our standard RCP forcing to test the effect of ice-Earth-sea level feedbacks on future projections. We find the effects on equivalent sea-level rise are quite small on timescales of a few centuries and similar to those using the ELRA bed model, confirming that the use of the latter in our main ensembles (Fig. 1) is adequate.

CESM-ice sheet simulations

Two additional ice sheet simulations are run using future atmospheric and oceanic forcing provided by two different RCP8.5 simulations described in ref.[43] and using the NCAR CESM 1.2.2 GCM with CAM5 atmospheric physics[88]. Ice sheet model physics and parameter values are identical in both simulations. Hydrofracturing (CALVLIQ) and cliff calving (VCLIFF) parameters use calibrated ensemble averages of 107 m^{-1} yr^{2} and 7.7 km yr^{-1}, consistent with the RCM-driven simulations shown in Figs. 2 and 3. The standard RCP8.5 simulation ignores future Antarctic meltwater and dynamic discharge, while an alternative simulation accounts for time-evolving and spatially resolved liquid water and solid ice inputs around the Antarctic margin, (peaking at >2 Sv in the early 22nd century) provided by an offline RCP8.5 ice-sheet simulation including hydrofracturing and ice-cliff calving[43]. The evolving temperature and precipitation fields from CESM are spatially interpolated and lapse-rate adjusted to the ice sheet model grid, using the same surface mass balance scheme used in our main RCM-forced ensembles. Similarly, sub-ice melt rates from CESM are calculated in exactly the same way as those provided by CCSM4 in our main ensembles. While this discrete two-step coupling between CESM and the ice sheet model does not account for time-continuous, fully coupled ice-ocean-climate feedbacks, the two simulations (with vs. without ice sheet discharge) span the envelope of possible outcomes when two-way meltwater feedback is fully accounted for. The two simulations using CESM with and without meltwater feedback are shown in Fig. 1h for comparison with our main RCM/CCSM4-forced ensembles.

Data availability. The data that support these findings, including all time-evolving ice sheet mass changes in the Pliocene, LIG and future model ensembles are freely available online and from the corresponding author upon reasonable request.

Code availability. Ice sheet and climate model codes associated with this reaseach are available from the corresponding author upon reasonable request.

Supplementary Information is available for this paper.

Acknowledgements We thank T. Naish for guidance on Pliocene sea level targets. This research was supported by the NSF under award ICER 1664013 and by a grant to the NASA Sea Level Change Team 80NSSC17K0698.

Author Contributions R.M.D. and D.P. conceived the model experiments and developed the main model codes with conceptual input from R.B.A. R.M.D. and D.P. wrote the manuscript with input from R.B.A., I.V., E.G., N.G., and S.S.. I.V. provided GRACE mass change estimates, E.G. contributed to ocean and atmospheric forcing scenarios, S.S. and A.C. provided CESM climatologies, N.G. collaborated on coupled ice-Earth simulations, A.D. provided paleo sea-level target ranges, D.L. compiled CMIP5 and CMIP6 GCM results, and D.M.G., E.A., and R.E.K. developed the statistical model described in Supplementary Information.

Author Information Reprints and permissions information is available at www.nature.com/reprints. The authors declare no competing financial interests. Readers are welcome to comment on the online version of the paper. Correspondence and requests for materials should be addressed to R.M.D. (deconto@geo.umass.edu).

Methods References

51 Pollard, D. & DeConto, R. Description of a hybrid ice sheet-shelf model, and application to Antarctica. *Geoscientific Model Development* **5**, 1273-1295 (2012).

52 Pollard, D. & DeConto, R. M. A simple inverse method for the distribution of basal sliding coefficients under ice sheets, applied to Antarctica. *The Cryosphere* **6**, 953-971 (2012).

53 Fretwell, P. *et al.* Bedmap2: Improved ice bed, surface and thickness datasets for Antarctica. *Cryosphere* **7**, 375-393 (2013).

54 Holland, P. R., Jenkins, A. & Holland, D. The response of ice shelf basal melting to variations in ocean temperature. *Journal of Climate* **21**, 2558-2572 (2008).

55 Pollard, D., Chang, W., Haran, M., Applegate, P. & DeConto, R. Large ensemble modeling of last deglacial retreat of the West Antarctic ice sheet: Comparison of simple and advanced statistical techniques. *Geoscientific Model Developmet* **9**, 1697-1723. (2016).

56 Rignot, E., Jacobs, S., Mouginot, J. & Scheuchl, B. Ice shelf melting around Antarctica. *Science* **314**, 266-270 (2013).

57 Schmidtko, S., Heywood, K. J., Thompson, A. F. & Aoki, S. Multidecadal warming of Antarctic waters. *Science* **346**, 1227-1231 (2014).

58 Nick, F. M., Van der Veen, C. J., Vieli, A. & Benn, D. I. A physically based calving model applied to marine outlet glaciers and implications for the glacier dynamics. *Journal of Glaciology* **56**, 781-794 (2010).

59 Tsai, C.-Y., Forest, C. E. & Pollard, D. The role of internal climate variability in projecting Antarctica's contribution to future sea-level rise. *Climate Dynamics* **55**, 1875-1892 (2020).

60 Benn, D. I., Warren, C. R. & Mottram, R. H. E.-S. R., 82, 143-179 (2007). Calving processes and the dynamics of calving glaciers. *Earth-Science Reviews* **82**, 143-179 (2007).

61 Ma, Y., Tripathy, C. S. & Bassis, J. N. Bounds on the calving cliff height of marine terminating glaciers. *Geophysical Research Letters* **44**, 1369-1375 (2017).

62 Robel, A. A. Thinning sea ice weakens buttressing force of iceberg mélange and promotes calving. *Nature Communications* **8**, 14596 (2017).

63 Joughin, I., Shean, D. E., Smith, B. E. & Floricioiu, D. A decade of variability on Jakobshavn Isbræ: Ocean temperatures pace speed through influence on mélange rigidity. *The Cryosphere* **14**, 211-227 (2020).

64 Pollard, D., DeConto, R. M. & Alley, R. B. A continuum model (PSUMEL1) of ice mélange and its role during retreat of the Antarctic Ice Sheet. *Geosci. Model Dev.* **11**, 5149-5172 (2018).

65 Locarnini, R. A. *et al.* World Ocean Atlas 2013, volume 1: Temperature. 40 (2013).

66 Bindschadler, R. A. *et al.* Ice-sheet model sensitivities to environmental forcing and their use in projecting future sea level (the SeaRISE project). *Journal of Glaciology* **59**, 195-224 (2013).

67 Le Brocq, A., Payne, A. J. & Vieli, A. An improved Antarctic dataset for high resolution numerical ice sheet models (albmap v1). *Earth System Science Data* **2**, 247–260 (2010).

68 Jenkins, A. *et al.* West Antarctic ice sheet retreat in the amundsen sea driven by decadal oceanic variability. *Nature Geoscience* **11**, 733-738 (2018).

69 Whitehouse, P. L., Bentley, M. J., Milne, G. A., King, M. A. & Thomas, I. D. A new glacial isostatic adjustment model for Antarctica: Calibrated and tested using observations of relative sea-level change and present-day uplift rates. *Geophysical Journal International* **190**, 1464-1482 (2012).

70 Ivins, E. R. *et al.* Antarctic contribution to sea level rise observed by grace with improved gia correction. *Journal of Geophysical Research: Solid Earth* **118**, 3126-3141 (2013).

71 A, G., Wahr, J. & Zhong, S. Computations of the viscoelastic response of a 3-d compressible earth to surface loading: An application to glacial isostatic adjustment in Antarctica and canada. *Geophysical Journal International* **192**, 557-572 (2013).

72 Capron, E. *et al.* Temporal and spatial structure of multi-millennial temperature changes at high latitudes during the last interglacial. *Quaternary Science Reviews* **1-3**, 116-133 (2014).

73 Clark, P. U. *et al.* Oceanic forcing of penultimate deglacial and last interglacial sea-level rise. *Nature* **577**, 660-664 (2020).

74 Austermann, J., Mitrovica, J. X., Huybers, P. & Rovere, A. Detection of a dynamic topography signal in last interglacial sea-level records. *Science Advances* **3** (2017).

75 Goelzer, H., Huybrechts, P., Loutre, M.-F. & Fichefet, T. Last interglacial climate and sea-level evolution from a coupled ice sheet–climate model. *Climate of the Past* **12**, 2195-2213 (2016).

76 Helsen, M. M., van de Berg, W. J., van de Wal, R. S. W., van den Broeke, M. R. & Oerlemans, J. Coupled regional climate-ice-sheet simulation shows limited Greenland ice loss during the eemian. *Clim. Past* **9**, 1773-1788 (2013).

77 Dahl-Jensen, D. & Neem. Eemian interglacial reconstructed from a Greenland folded ice core. *Nature* **493**, 489-494 (2013).

78 Nicholl, J. A. L. *et al.* A laurentide outburst flooding event during the last interglacial period. *Nature Geosci* **5**, 901-904 (2012).

79 Pal, J. S. *et al.* Regional climate modeling for the developing world – the ICTP RegCM3 and regcnet. *Bulletin of the American Meteorological Society* **88(9)**, 1395-1409 (2007).

80 Shields, C. A. & Kiehl, J. T. Simulating the pineapple express in the half degree Community Climate System Model, ccsm4. *Geophysical Research Letters* **43**, 7767-7773 (2016).

81 van Wessem, J. M. *et al.* Updated cloud physics in a regional atmospheric climate model improves the modelled surface energy balance of Antarctica. *The Cryosphere* **8**, 125-135 (2014).

82 Lenaerts, J. T. M., Vizcaino, M., Fyke, J., van Kampenhout, L. & van den Broeke, M. R. Present-day and future Antarctic ice sheet climate and surface mass balance in the community earth system model. *Climate Dynamics* **47**, 1367-1381 (2016).

83 Meinshausen, N. *et al.* The RCP greenhouse gas concentrations and their extensions from 1765 to 2300. *Climatic Change* **109**, 213-241 (2011).

84 Morelli, A. & Danesi, S. Seismological imaging of the Antarctic continental lithosphere: A review. *Global and Planetary Change* **42**, 155-165 (2004).

85 Heeszel, D. S. *et al.* Upper mantle structure of Central and West Antarctica from array analysis of rayleigh wave phase velocities. *Journal of Geophysical Research: Solid Earth* **121**, 1758-1775 (2016).

86 Nield, G. A. *et al.* Rapid bedrock uplift in the Antarctic Peninsula explained by viscoelastic response to recent ice unloading. *Earth and Planetary Science Letters* **397**, 32-41 (2014).

87 Zhao, C. *et al.* Rapid ice unloading in the fleming glacier region, southern Antarctic Peninsula, and its effect on bedrock uplift rates. *Earth and Planetary Science Letters* **473**, 164-176 (2017).

88 Hurrell, J. W. *et al.* The Community Earth System Model: A framework for collaborative research. *Bulletin of the American Meteorological Society* **94**, 1339-1360 (2013).

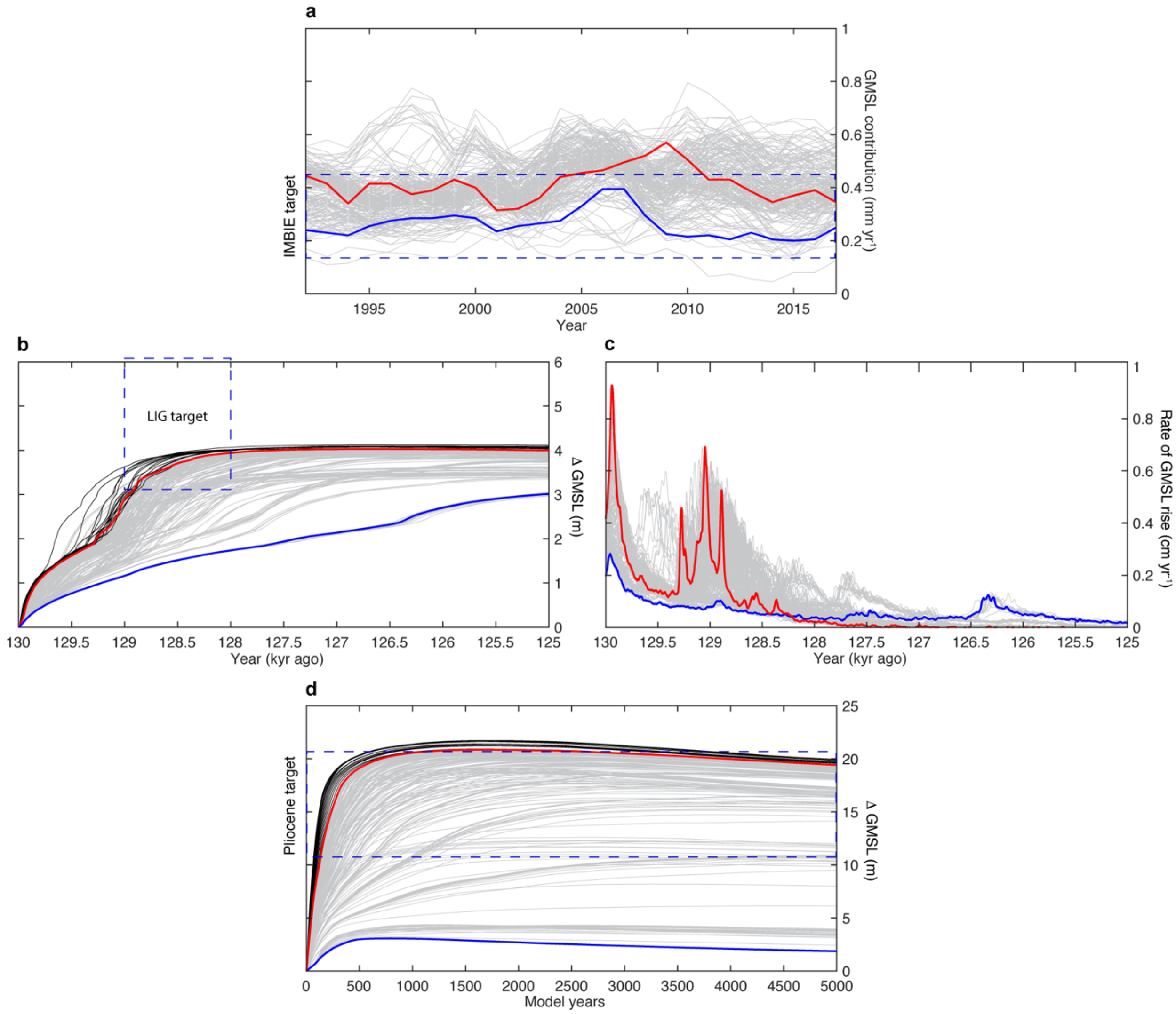

Extended Data Figure 1 | Ensemble targets. 196 simulations (grey lines), each using a unique combination of hydrofracturing and ice-cliff calving parameters (Extended Data Table 1) are compared with observational targets (blue dashed boxes). Solid blue lines show simulations without hydrofracturing and ice-cliff calving. Red lines show the simulations with the maximum parameter values in our main ensemble. Additional simulations (black lines) allow ice-cliff calving rates up to 26 km yr^{-1}, twice the maximum value used in our main ensembles (Extended Data Table 1). Vertical heights of blue boxes represent the likely range of observations. Changes in ice mass above floatation are shown in equivalent GMSL. **a**, Simulated annual contributions to GMSL in the RCP8.5 ensemble compared with the 1992-2017 IMBIE[1] observational average (dashed blue box). **b**, LIG ensemble simulations from 130 ka to 125 ka. The height of the dashed blue box shows the LIG target range (3.1-6.1 m), while the width represents the ~1000-year age uncertainty of the sea level data[32]. **c**, The same LIG simulations in **b**, except showing the rate of GMSL change contributed by Antarctica, smoothed over a 25-year window. The initial peak in the early LIG is mainly caused by the loss of vulnerable marine-based ice in West Antarctica. Sustained LIG contributions to GMSL rise are <1 cm yr^{-1}. **d**, The same as **b** except for warmer mid-Pliocene conditions. Maximum ice loss is compared with observational estimates of 11-21 m[33,34] (dashed blue lines). Note the saturation of simulated GMSL values near the top of the LIG and Pliocene ensemble range, and the failure of the model to produce realistic LIG or Pliocene sea level without hydrofracturing and ice-cliff calving processes enabled (blue lines).

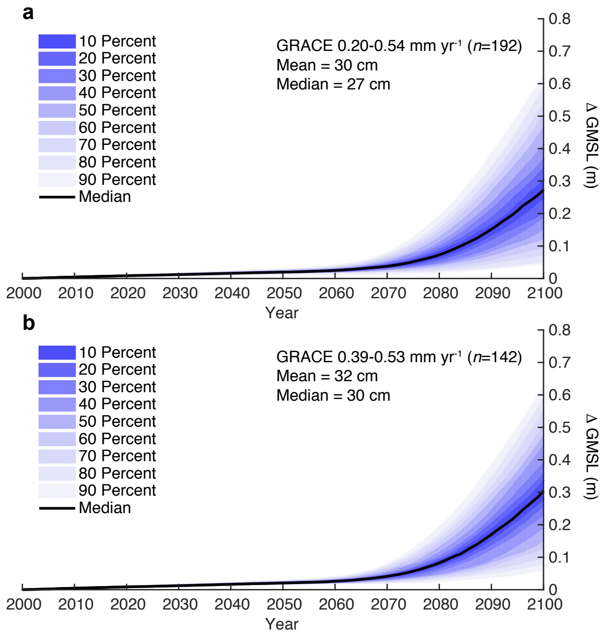

Extended Data Figure 2 | RCP8.5 calibrated ensembles using alternative GRACE estimates of ice mass change. The fan charts show the time-evolving uncertainty and range around the median ensemble value (black line) in 10% increments. RCP8.5 ice sheet model ensembles calibrated with GRACE estimates of annual mass change averaged from 2002-2017, using alternative GIA corrections (see Methods). **a**, Using GIA corrections producing estimates of mass loss between 2002 and 2017 of 0.2-0.54 mm yr^{-1} and **b**, 0.39-0.53 mm yr^{-1}. The more restrictive and higher range of GRACE estimates in **b** skews the distribution and shifts the ensemble median values of GMSL upward from 27 cm to 30 cm in 2100 and from 4.44 m to 4.94 m in 2200.

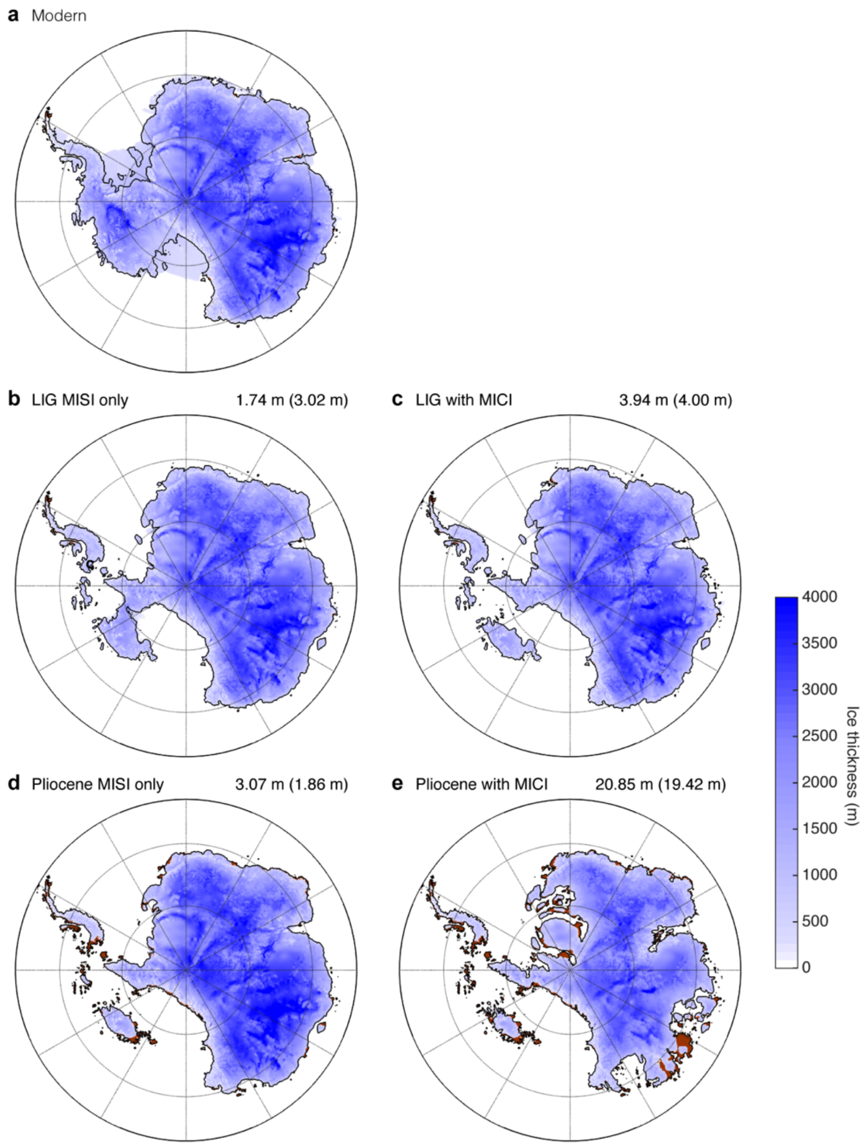

Extended Data Figure 3 | Last Interglacial and Pliocene ice sheet simulations. Ice sheet simulations with the updated model physics used in our future ensembles and driven with the same LIG and Pliocene climate forcing used in ref.[8]. Simulations without hydrofracturing and ice-cliff calving (left panels) correspond to blue lines in Extended Data Figure 1. Simulations using maximum hydrofracturing and ice-cliff calving parameters used in our ensembles (right panels) correspond to red lines in Extended Data Figure 1. **a**, Modern (1950) ice sheet simulation. **b**, **c**, LIG simulations run from 130 ka to 125 ka are shown at 125 ka. Values at the top of each panel are the maximum GMSL contribution between 129 ka and 128 ka. Values in parentheses are the GMSL contribution at 125 ka. **d**, **e**, Warm Pliocene simulations. Values shown are the maximum GMSL achieved during the simulations. Smaller values in parentheses show GMSL contributions after 5000 model years (Extended Data Figure 2d). Ice mass gain after peak retreat is caused by a combination of post-retreat bedrock rebound and enhanced precipitation in the warm Pliocene atmosphere.

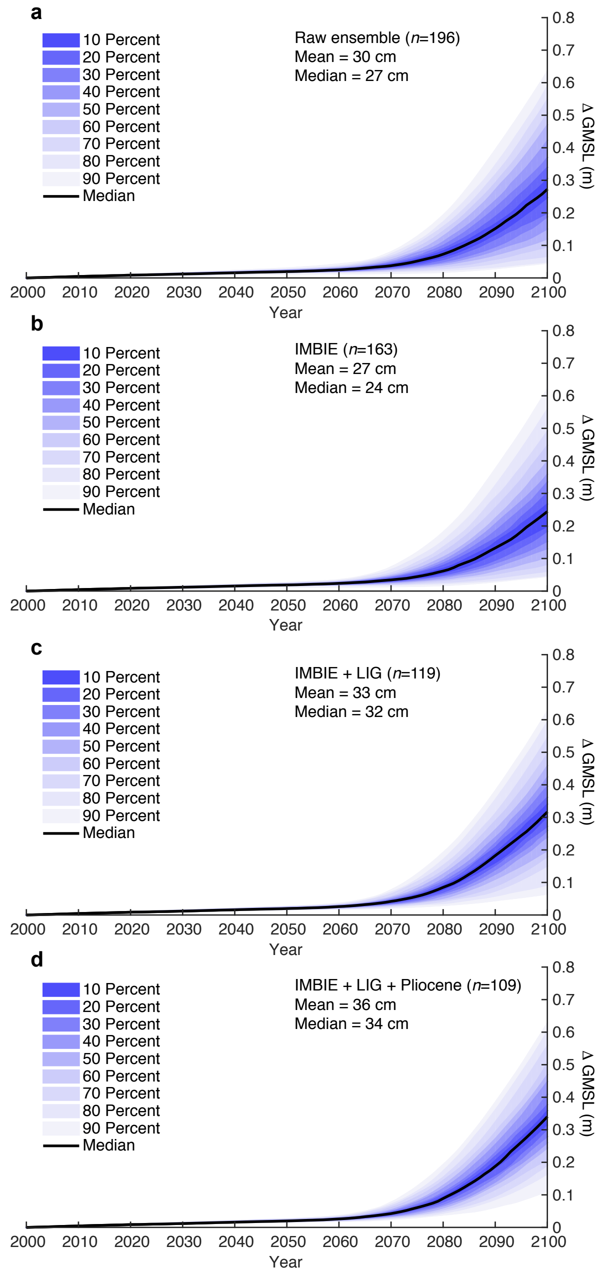

Extended Data Figure 4 | RCP8.5 ensembles calibrated with modern and paleo observations. The fan charts show the time-evolving uncertainty and range around the median ensemble value (black line) in 10% increments. Mean and median ensemble values are shown at 2100. **a**, Raw ensemble with a range of plausible model parameters based on glaciological observations (Extended Data Table 1). **b**, The ensemble trimmed with IMBIE[1] (1992-2017) estimates of ice mass change. **c**, The ensemble trimmed with IMBIE rates of ice mass change plus LIG sea level constraints between 129 ka and 128 ka[32]. **d**, The same as **c**, except with the addition of maximum mid-Pliocene sea-level constraints[33,34] (Extended Data Figure 1). Future ensembles in the main text (Fig. 1, Table 1) use the combined IMBIE + LIG + Pliocene history matching constraints as shown in **d.**

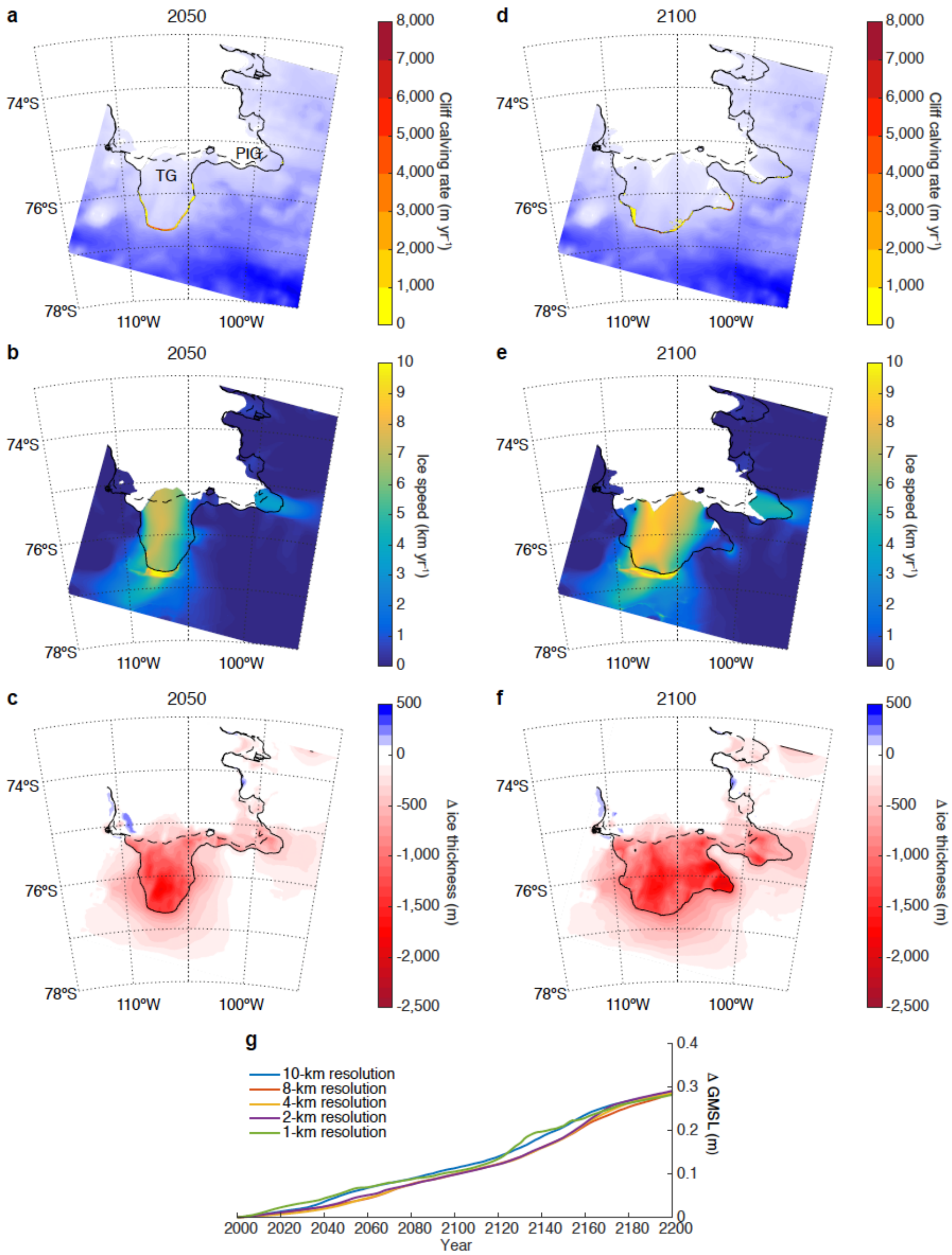

Extended Data Figure 5 | Future retreat of Thwaites Glacier (TG) and Pine Island Glacier (PIG) with +3 °C global warming. The Amundsen Sea sector of the ice sheet in a nested, high resolution (1 km) simulation using average calibrated values of hydrofracturing and ice-cliff calving parameters (CALVLIQ=107 m^{-1} yr^2; VCLIF=7.7 km yr^{-1}), consistent with those used in CESM1.2.2-forced simulations (Fig. 1h) and CDR simulations (Fig. 3, Table 2). **a-c**, The ice sheet in 2050. **d-f**, The ice sheet in 2100. **a** and **d**, Ice sheet geometry and annually averaged ice-cliff calving rates at thick, weakly buttressed grounding lines. The solid line in all panels is the grounding line and the dashed line is its initial position. Note that simulated ice-cliff calving rates are generally much slower than the maximum allowable value of 7.7 km yr^{-1}. Ice shelves downstream of calving ice cliffs are the equivalent of weak mélange, incapable of stopping calving[64]. **b** and **e**, Ice surface speed showing the location of streaming ice and fast flow just upstream of calving ice cliffs where driving stresses are greatest. **c** and **f**, Change in ice thickness relative to the initial state. **g**, GMSL contributions within the nested domain at model spatial resolutions spanning 1 to 10 km.

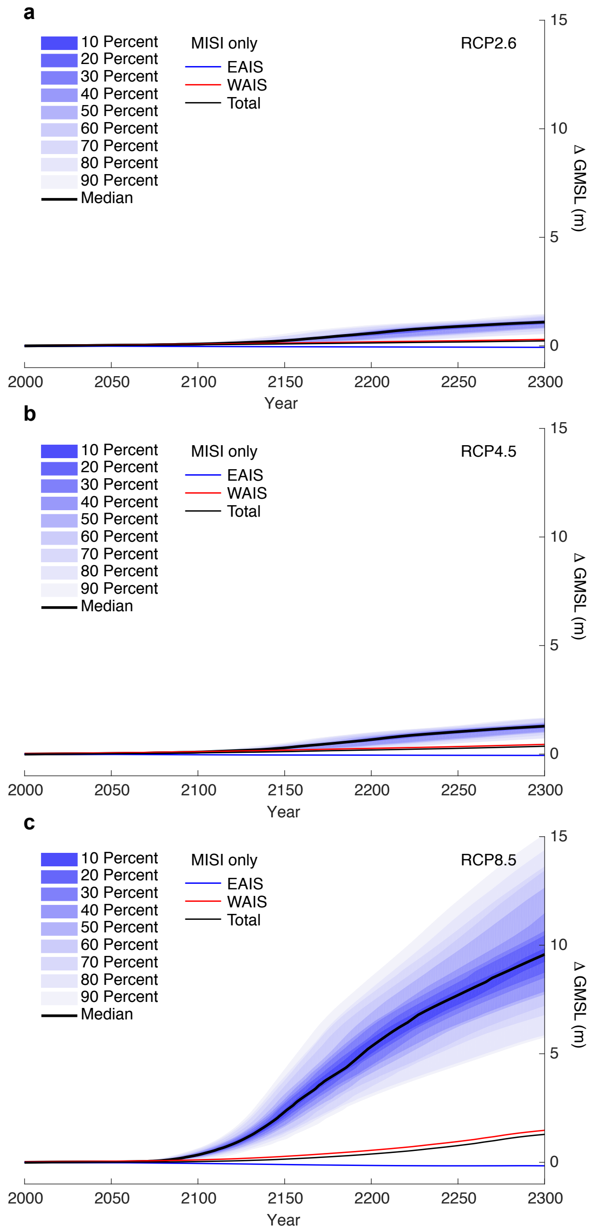

Extended Data Figure 6 | Antarctic contribution to sea level under standard RCP forcing. The fan charts show the time-evolving uncertainty and range around the median ensemble value (thick black line) in 10% increments. The RCP ensembles use the same IMBIE, LIG, and Pliocene observational constraints applied to the simulations in Fig. 1. GMSL contributions in simulations without hydrofracturing or ice-cliff calving (excluded from the validated ensembles) are shown for East Antarctica (thin blue line), West Antarctica (thin red line), and the total Antarctic GMSL contribution (thin black line). **a,** RCP2.6, **b,** RCP4.5, and **c,** RCP8.5.

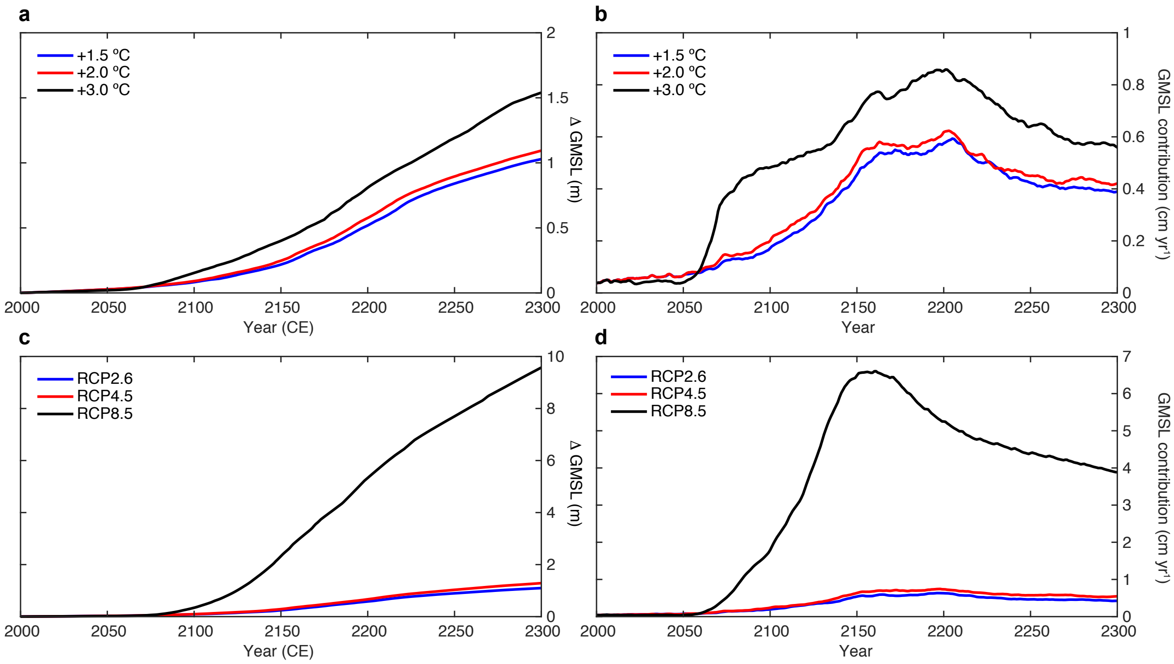

Extended Data Figure 7 | Long term magnitudes and rates of GMSL rise contributed by Antarctica. a, Ensemble median (50th percentile) projections of GMSL rise contributed by Antarctica with emissions forcing consistent with +1.5 ºC and +2.0 ºC Paris Climate Agreement ambitions, versus a +3.0 ºC scenario closer to current NDCs. **b**, Median (50th percentile) rates of GMSL rise in the same emissions scenarios in **a**, illustrating a sharp jump in ice loss in the warmer +3.0 ºC scenario after 2060 (also see Fig. 1), and reduced net ice loss before 2060 (black line) caused by increased snowfall. **c,** Ensemble median (50th percentile) projections of GMSL rise contributed by Antarctica with emissions forcing consistent with standard RCP scenarios, highlighting the potential for extreme GMSL rise under very high emissions (RCP8.5). **d**, Ensemble median (50th percentile) rates of GMSL rise in the same RCP scenarios shown in **c**. Note the much larger y-axis scales in **c** and **d** relative to **a** and **b**.

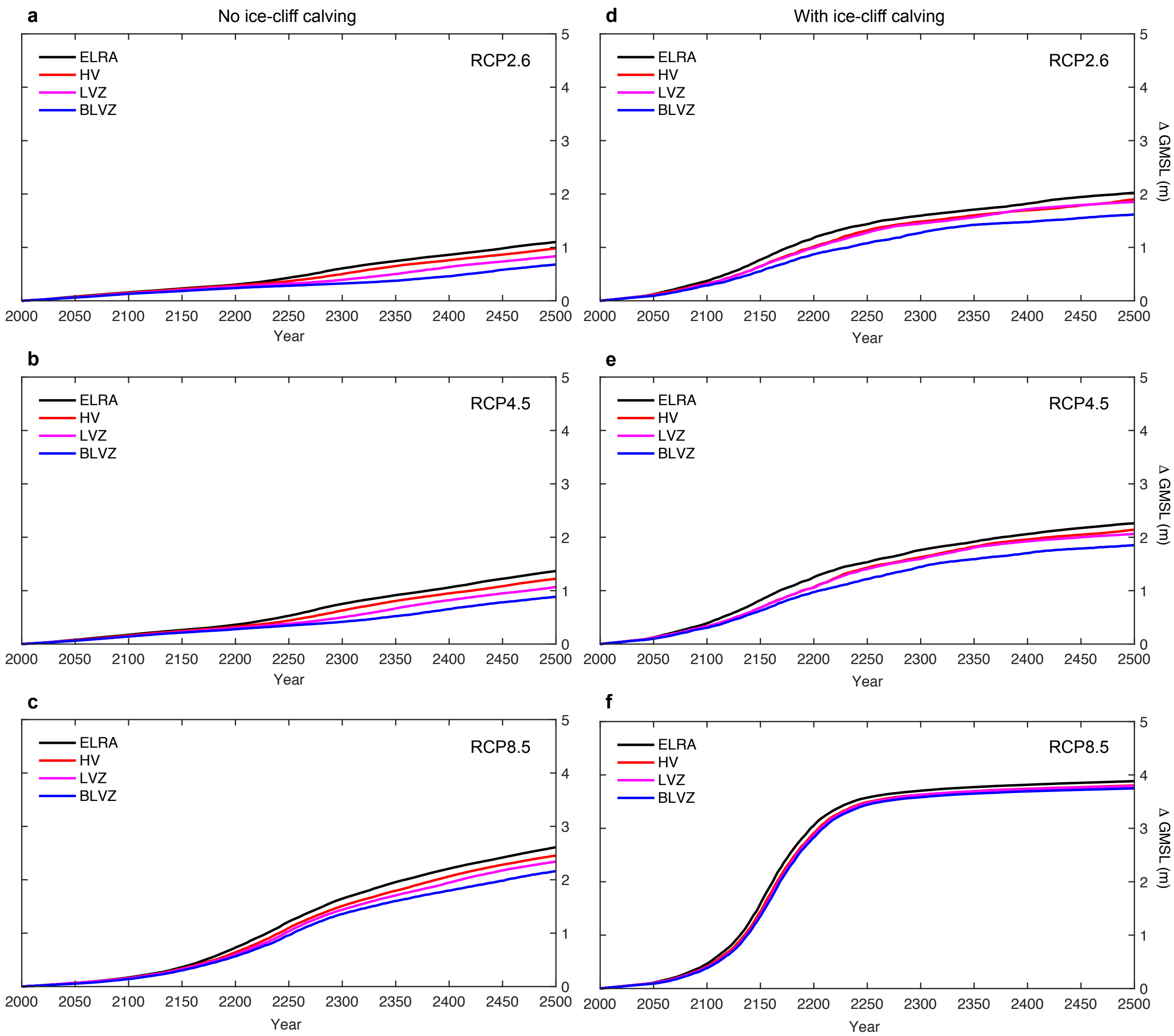

Extended Data Figure 8 | Coupled ice-Earth-sea level model simulations. Simulations without hydrofracturing and ice-cliff calving processes are shown in the left column. Simulations with hydrofracturing and ice-cliff calving enabled are shown at right. GMSL contributions are from WAIS only. Various Earth viscosity profiles (colored lines) are compared with the ice sheet model's standard ELRA formulation (black line). The most extreme viscosity profile (blue line) assumes a thin lithosphere and very weak underlying mantle, like that observed in the Amundsen sea[47], but extended continent-wide. **a**, RCP2.6 without hydrofracturing or ice-cliff calving. **b**, RCP2.6 with hydrofracturing and ice-cliff calving. **c**, RCP4.5 without hydrofracturing or ice-cliff calving. **d**, RCP4.5 with hydrofracturing and ice-cliff calving. **e**, RCP8.5 without hydrofracturing or ice-cliff calving. **f**, RCP8.5 with hydrofracturing and ice-cliff calving.

Extended Data Table 1 | Model ensemble parameter values

Meltwater crevassing parameter, CALVLIQ (m^{-1} yr^{2})	Maximum calving rate, VCLIFF (km yr^{-1})
0	0
15	1
30	2
45	3
60	4
75	5
90	6
105	7
120	8
135	9
150	10
165	11
180	12
195	13

Parameter values used in unique combinations to generate 196 model ensemble members. Blue and red values correspond to blue and red simulations in Extended Data Figure 1. Thirteen additional combinations extending CALVLIQ to 390 m^{-1} yr^{2} and VCLIFF to 26 km yr^{-1} are shown in black in Extended Data Figure 1. Average calibrated parameter values based on IMBIE, LIG, and Pliocene history matching (Extended Data Figure 1) are CALVLIQ=107 m^{-1} yr^{2}, and VCLIFF=7.7 km yr^{-1}. Corresponding median values are 105 m^{-1} yr^{2} and 7 km yr^{-1}.

Extended Data Table 2 | Antarctic sea level contributions with alternative maximum ice-cliff calving rates

Scenario	2100	2200	2300
+1.5ºC (13 km yr^{-1})	0.08 (0.06-0.10)	0.52 (0.22-0.77)	1.03 (0.61-1.22)
+1.5ºC (11 km yr^{-1})	0.08 (0.06-0.90)	0.48 (0.22-0.59)	0.98 (0.61-1.08)
+1.5ºC (8 km yr^{-1})	0.08 (0.06-0.90)	0.44 (0.18-0.55)	0.95 (0.48-1.04)
+2.0 ºC (13 km yr^{-1})	0.09 (0.07-0.11)	0.58 (0.26-0.83)	1.09 (0.68-1.25)
+2.0 ºC (11 km yr^{-1})	0.09 (0.07-0.10)	0.52 (0.25-0.63)	1.05 (0.67-1.16)
+2.0 ºC (8 km yr^{-1})	0.09 (0.07-0.11)	0.58 (0.26-0.83)	1.09 (0.68-1.25)
+3.0 ºC (13 km yr^{-1})	0.15 (0.08-0.27)	0.81 (0.45-1.25)	1.54 (1.04-2.03)
+3.0 ºC (11 km yr^{-1})	0.14 (0.08-0.23)	0.71 (0.43-1.09)	1.43 (0.99-1.83)
+3.0 ºC (8 km yr^{-1})	0.14 (0.08-0.20)	0.67 (0.41-1.00)	1.40 (0.94-1.75)
RCP2.6 (13 km yr^{-1})	0.09 (0.07-0.12)	0.58 (0.27-0.85)	1.10 (0.71-1.36)
RCP2.6 (11 km yr^{-1})	0.08 (0.07-0.10)	0.52 (0.27-0.67)	1.07 (0.71-1.17)
RCP2.6 (8 km yr^{-1})	0.08 (0.07-0.09)	0.48 (0.23-0.60)	1.00 (0.58-1.11)
RCP4.5 (13 km yr^{-1})	0.09 (0.07-0.12)	0.67 (0.35-0.91)	1.29 (0.90-1.59)
RCP4.5 (11 km yr^{-1})	0.09 (0.07-0.11)	0.64 (0.34-0.78)	1.26 (0.89-1.40)
RCP4.5 (8 km yr^{-1})	0.09 (0.07-0.11)	0.57 (0.30-0.70)	1.20 (0.75-1.32)
RCP8.5 (13 km yr^{-1})	0.34 (0.20-0.53)	5.33 (3.70-7.64)	9.57 (6.87-13.55)
RCP8.5 (11 km yr^{-1})	0.31 (0.19-0.47)	4.96 (3.49-6.38)	8.80 (6.77-11.66)
RCP8.5 (8 km yr^{-1})	0.30 (0.20-0.43)	4.41 (3.20-5.71)	8.10 (5.88-9.73)

Ensemble median GMSL contributions using IMBIE, Last Interglacial, and Pliocene observational constraints in meters relative to 2000. Values in parentheses are the 17th-83rd percentiles (likely range). Scenarios refer to the maximum global mean temperature reached relative to pre-industrial (1850) or following extended RCPs, and with the upper bound of the ice-cliff calving parameter (VCLIFF) set at the maximum observed value of 13 km yr^{-1} (n=196; Table 1), or alternatively at 11 km yr^{-1} (n=168) or 8 km yr^{-1} (n=126; Extended Data Table 1). Reducing the upper bound of the ice cliff calving parameter has a relatively small impact on ensemble medians, especially in the near term. The average calibrated value of VCLIFF constrained by observational constraints is 7.7 km yr^{-1} which explains the severe truncation of the upper tail of the distributions when using 8 km yr^{-1} as the sampling limit.

Supplementary Information
The Paris Climate Agreement and future sea level rise from Antarctica

*Robert M. DeConto, David Pollard, Richard B. Alley, Isabella Velicogna, Edward Gasson, Natalya Gomez, Shaina Sadai, Alan Condron, Daniel M. Gilford, Erica L. Ashe, Robert E. Kopp, Dawei Li, and Andrea Dutton.

Uncertainty in surface melt rates and climate forcing

As discussed in the main text and Methods, our ice sheet model accounts for rain and meltwater-induced wet crevassing and hydrofracturing that can trigger the sudden loss of buttressing ice shelves, as mean summer temperatures approach and exceed -1ºC. As a result, our future simulations (Fig. 1) are sensitive to the timing when substantial quantities of liquid water appear on vulnerable ice shelf surfaces. In our prior work[1], RCP8.5 climate forcing used to run future ice sheet simulations produced substantially more melt than indicated by an independent study[2], using different regional and global climate models. Here, we compare the updated climate forcing used in this study with those produced by the CMIP5 GCMs used in ref-[2] and 22 state-of-the-art CMIP6 GCMs[3].

Surface melt rates produced by the climate models used in this study (Supplementary Figure 1) are only ~25% as high as those in our previous modeling[1], but they remain somewhat higher (especially around the East Antarctic Margin) than those calculated by the empirical temperature-melt relationship used ref.-[2]. These differences are mainly due to atmospheric temperatures in our model being corrected to account for a cold bias of ~2.9 ºC in low elevations over ice surfaces relative to observations[4]. Similar cold biases of ~2.3 and ~2.4 ºC, caused by a deficit of net longwave radiation, are found in the RACMO2 RCM forced by ERA-Interim reanalysis[5] and the CESM GCM[6]. Given the exponential relationship between melt and summer mean (DJF) surface temperature[2], our bias-corrected temperatures increase our future melt rates relative to those using uncorrected climate model temperatures, or those using RACMO2 as the bias-correction benchmark[2].

Additional relatively minor departures from ref-[2] are caused by different approaches used to calculate total surface melt from air temperatures. Here, melt rates are calculated by a box model[7], using positive degree days for snow and ice melt with standard coefficients[8], and accounting for partial refreezing of meltwater[1]. In our ice sheet model, total surface melt available to influence surface crevassing (Supplementary Figure 1) is the fraction of meltwater not refrozen in the near-surface, plus any rainwater. Under RCP8.5, rainwater in our calculations adds ~10% to total meltwater production in areas of high melt at the end of the 21st century.

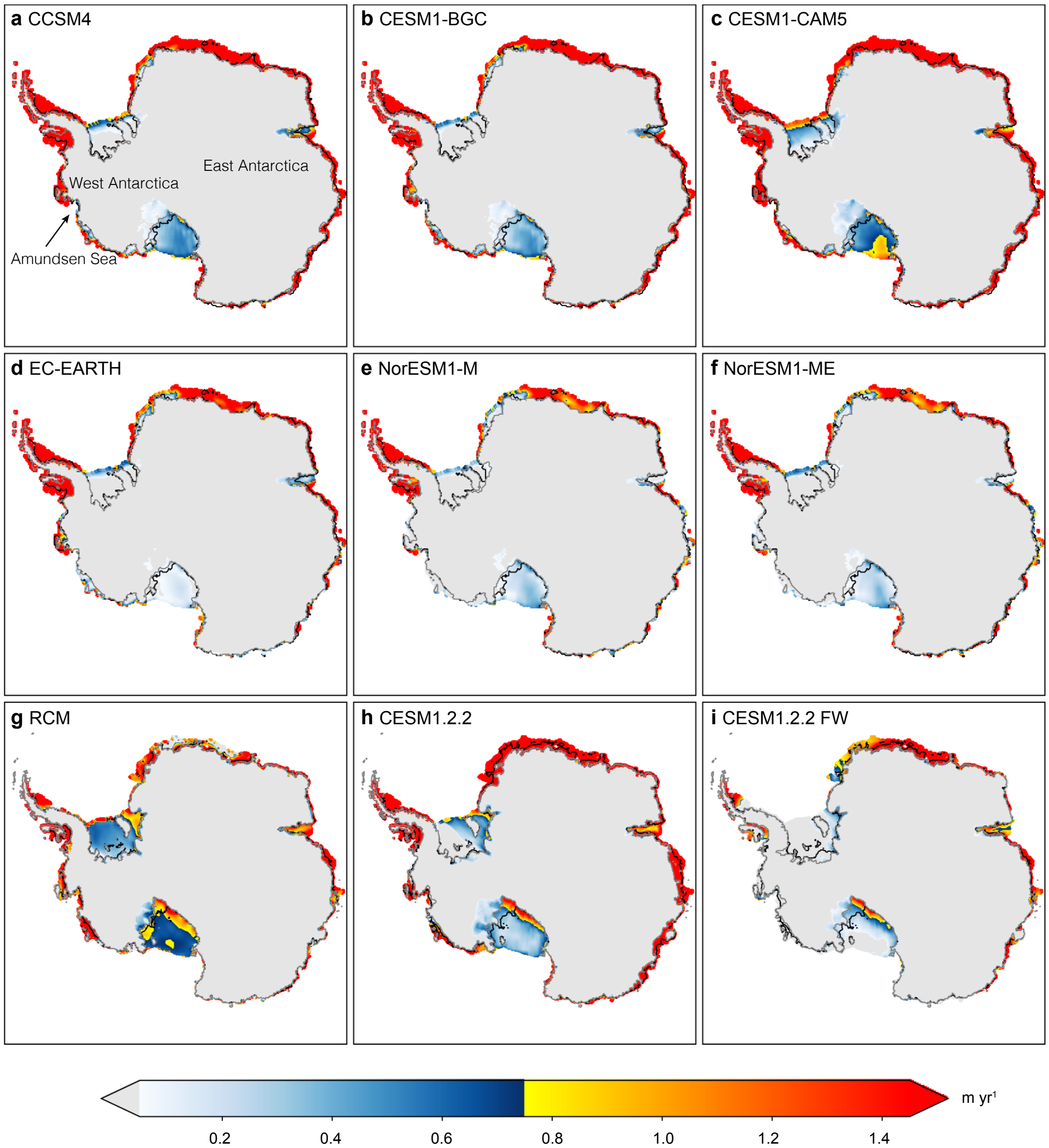

Supplementary Figure 1 | Comparison of surface melt and rainwater production rates. Surface water production rates (rain plus meltwater not refrozen in the near surface, m yr^{-1}) in the last decade of the 21st century under RCP8.5 emissions calculated by the surface mass balance scheme in our ice sheet model. **a-f**, Melt rates from six global climate models (GCMs)[9-13] used in a previous assessment[2] are compared with the climate models used in this study (**g-i**). **g-i**, Surface melt and rainwater rates produced by the regional climate model (RCM) and GCM used in this study. Spatial patterns differ among the climate models. There is more melt water produced on the Ross and Filchner-Ronne ice shelves in the RCM relative to the other models, but the RCM shows less warming over the Amundsen Sea and most of the East Antarctic margin. The two CESM1.2.2 simulations either ignore (**h**) or include (**i**) meltwater (freshwater and iceberg discharge) feedbacks between the GCM and ice sheet model (Fig. 1f). As discussed in the main text, the smaller melt rates in **i** are the result of a strong negative atmospheric warming feedback caused by sea ice expansion when ice sheet discharge is accounted for in the GCM[14]. The blue to yellow transition in the color bar (750 mm yr^{-1}) is the approximate meltwater production rate preceding the breakup of the Larsen B ice shelf in 2002[2]. Melt and rainwater required to break up thick (>600 m) ice shelves in our hydrofracturing model is closer to 1,400 mm yr $^{-1}$.

Here, we compare the timing of future summer warming over four regions of the Antarctic margin (Supplementary Figure 2) simulated by the RCM used to force our main ice sheet model ensembles under RCP8.5 (Fig. 1g,h) relative to ERA5 reanalysis[15], five CMIP5 climate models following RCP8.5 used in a previous assessment of future surface melt trajectories[2], and 22 CMIP6 GCMs[3] following SSP5-85[16]. The regions include three major buttressing ice shelves (Larsen, Ross, Filcher-Ronne), and the Amundsen Sea, where weakly buttressed outlet glaciers, including Thwaites Glacier, are currently thinning and retreating[17]. The CMIP6 models sampled here include ACCESS-CM2, ACCESS-ESM1-5, BCC-CSM2-MR, CAMS-CSM1-0, CanESM5, CESM2, CESM2-WACCM, EC-Earth3, EC-Earth3-Veg, FGOALS-f3-L, FIO-ESM-2-0, GFDL-CM4, GFDL-ESM4, INM-CM4-8, INM-CM5-0, IPSL-CM6A-LR, MIROC6, MPI-ESM1-2-HR, MPI-ESM1-2-LR, MRI-ESM2-0, NESM3, NorESM2-LM. This comparison places the climate forcing used in our ice sheet simulations within the context of other state-of-the-art climate models, including a variant of CESM (CESM1.2.2-CAM5) used to test the importance of climate-ice sheet feedbacks in Figure 1h. We focus on the summer melt season, because of its connection to ice-shelf breakup.

The evolution of atmospheric warming in the RCM used in our main ensembles (using CCSM4 ocean boundary conditions) is comparable to the subset of CMIP5 GCMs[2]. When global mean temperatures reach +1.5 ºC, +2.0 ºC, and +3.0 ºC, warming averaged over Antarctica is slightly lagged, reaching +1.48, ºC, +1.50 ºC, and +1.82 ºC, respectively. Both the RCM and CESM1.2.2 used in our study are considerably colder than ERA5 and most CMIP6 GCMs over the main ice shelves. Summer temperatures over the sensitive Larsen and Amundsen Sea regions approach the threshold for producing extensive rain and surface meltwater faster in almost all of the CMIP6 GCMs than either the RCM or CESM1.2.2 (Supplementary Figure 2a-b).

Bias correcting the summer temperatures (T_{DJF}) in the climate models relative to the 40-year average of summer temperatures in ERA5 ($\hat{T}_{DJF}(t) = T_{DJF}(t) - \overline{T_{DJF}} + \overline{T_{DJF\ ERA5}}$), substantially reduces the range of simulated temperatures among the climate models, especially in the late 20th and early 21st centuries (Supplementary Figure 2e-h). However, we note that the range of bias-corrected temperatures among the models still expands markedly toward the end of the 21st century. Because of the strong cold bias around the periphery of Antarctica in CESM relative to both observations[6] and ERA5 (red vs. orange lines in Supplementary Figure 2), corrected temperatures in CESM (Supplementary Figure 2e-h) show more warming in 2100 than the median of the bias-corrected CMIP6 GCMs.

Clearly the wide range of warming rates simulated by these climate models, particularly among CMIP6 GCMs, represents considerable uncertainty in the timing when surface meltwater production and ice shelf loss might begin in the future. The quantified impact of this climatic uncertainty on our ice sheet projections should be explored in future work.

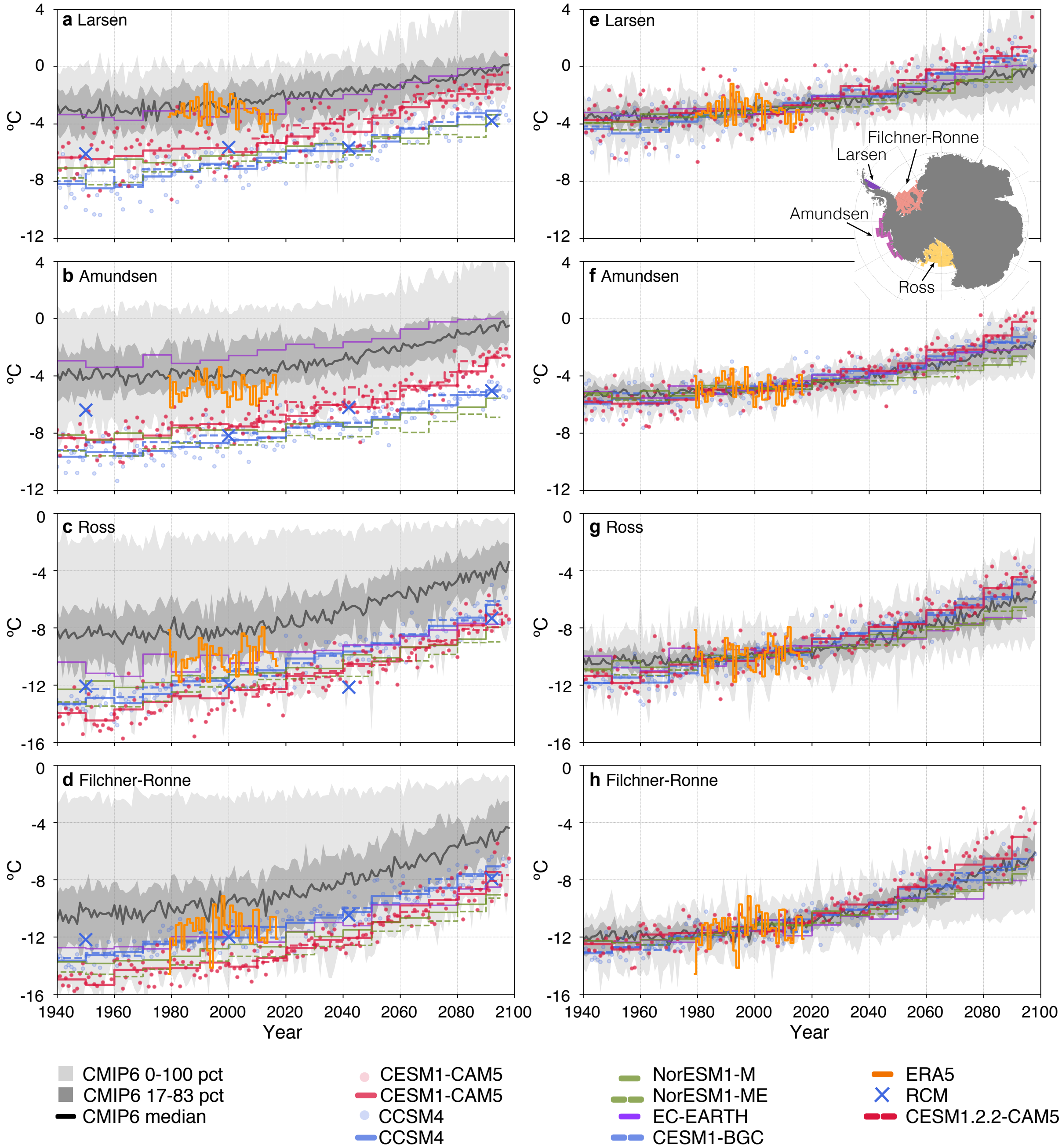

Supplementary Figure 2 | Future atmospheric warming over Antarctic ice shelves. Summer (DJF) surface (2-meter) air temperature (ºC) simulated by five CMIP5 and 22 CMIP6 global climate models (GCMs) over the period 1940-2100. CMIP5 models follow RCP8.5 emissions and CMIP6 models follow SSP5-85. GCM temperatures (averaged over 10-year intervals) are compared with ERA5 reanalysis (orange line), the RCM (RCP8.5) used in our main ensembles (blue crosses) and CESM1.2.2 (RCP8.5; red dashed line) used in ice sheet simulations shown in Figure 1h. The inset shows the model domains corresponding to the Larsen, Ross, and Filchner-Ronne ice shelves, and the Amundsen Sea sector of West Antarctica. **a-d**, Uncorrected, raw model temperatures averaged over the individual model domains. **e-h**, Bias corrected temperatures using ERA5. Blue crosses show the RCM temperatures at specific times (1950, 2000, and when effective atmospheric CO_2 reaches 2 and 4 times preindustrial levels).

Ice shelf hydrofracturing in compressional flow regimes

It is conceivable that in regions of compressional ice-shelf flow, liquid water flowing on the surface might tend to reach the margins and run off, instead of penetrating into crevasses and causing hydrofracture. This potential influence of compressional ice flow on hydrofracturing is tested by modifying the model's wet crevassing (hydrofracturing) scheme (see Methods). In this case, the total meltwater production rate R is reduced by ×0.1 as a function of the local ice convergence rate (yr^{-1}) at convergences >0.01, ramping to ×1 where convergence is zero.

We find that reducing wet crevasse penetration in regions of convergent flow has little influence on our continental-scale results (Supplementary Figure 3). In climate scenarios with minimal surface melt (RCP2.6), Antarctic ice loss is dominated by WAIS retreat in response to ocean-driven thinning of ice shelves and the associated reduction in buttressing. In such instances, the influence of hydrofracturing is minimal and modifications to our wet crevassing scheme are inconsequential. Under more extreme future warming scenarios (RCP8.5), shelf loss is largely driven by massive meltwater production and the sudden onset of widespread meltwater-enhanced calving (hydrofracturing). In the model, this hydrofracturing begins near the calving fronts where the ice is thinnest, convergence and buttressing are minimal[18], and air temperatures (melt rates) are highest. Once initiated, meltwater-induced calving reduces convergence and compressional flow in the ice upstream and the meltwater enhanced calving propagates, resulting in the complete loss of major ice shelves, despite the reduction of d_w in convergent flow regimes. Extending these results with a more sophisticated, physically based, time-dependent[19] hydrofracturing scheme is the subject of ongoing work. However, these results combined with the relatively high melt rates required to trigger destruction of ice shelves like the Larsen B, add confidence that the model formulation used in our main ensembles is reasonable.

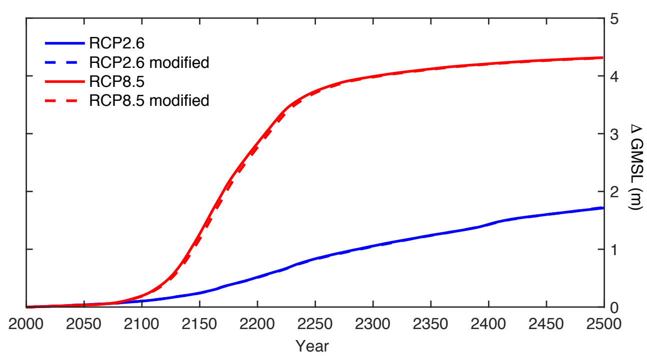

Supplementary Figure 3 | Global mean sea level contributions from Antarctica with a modified hydrofracturing scheme. Simulations follow two future greenhouse gas emissions scenarios, using our nominal model formulation of hydrofracturing used throughout the main text (solid lines), compared with an alternative formulation reducing meltwater influence on crevasse penetration in convergent (compressive) flow regimes (dashed lines).

Reformulation of buttressing at grounding lines

The hybrid ice sheet model used here heuristically blends vertically integrated shallow ice/shallow shelf approximations (SIA/SSA)[20], with the seaward ice flux at grounding lines imposed as a boundary condition according to an analytical expression relating ice flux to ice thickness[21]. This expression includes a term θ representing buttressing by ice shelves, i.e., the amount of back stress caused by pinning points or lateral forces on the ice shelf further downstream. The buttressing factor θ is defined as the ratio of vertically averaged horizontal deviatoric stress normal to the grounding line, relative to its value if the ice shelf was freely floating with no back stress.

The analysis for grounding-line flux and buttressing in ref.[6] is limited to one-dimensional flowline geometry. In our standard model[20], the expression is applied across individual one-grid-cell-wide segments separating pairs of grounded and floating grid cells, so that the orientation of each single-cell "grounding-line" segment is parallel to either the x or the y axis. Although this is consistent with the one-dimensional character of the formulation in ref.[21], it neglects the actual orientation of the real, slightly wider-scale grounding line, and results in non-isotropic θ values for u and v staggered-grid velocities.

Alternatively, a more rigorous, isotropic, treatment of θ can been implemented, by applying the expression in ref.[21] to normal flow across a more realistic grounding-line orientation not constrained to one or the other grid axes, following equations 2 and 6 in ref.[22] The alternative model treatments of θ are represented schematically by insets in Supplementary Figure 4a,b. We find that the new treatment of θ substantially improves the model's performance[23] in the idealized, relatively narrow fjord-like setting of the Marine Ice Sheet Model Intercomparison Project+ (MISMIP+)[24], with regards to the transient pace of grounding line retreat and re-advance when compared with models using higher order or full-stokes treatments of englacial stresses. Our new results fall well within the envelope of the multi-model range in the MISMIP+ intercomparison[24] (Supplementary Figure 4a,b). In contrast, at the continental scale the new, more rigorous treatment of θ has a very small effect on the pace of retreat (Supplementary Figure 4c,d), presumably because the dynamics of wide, major Antarctic outlets are adequately represented with the 1-dimensional formulation. The new treatment and further results are described in detail in ref.[23].

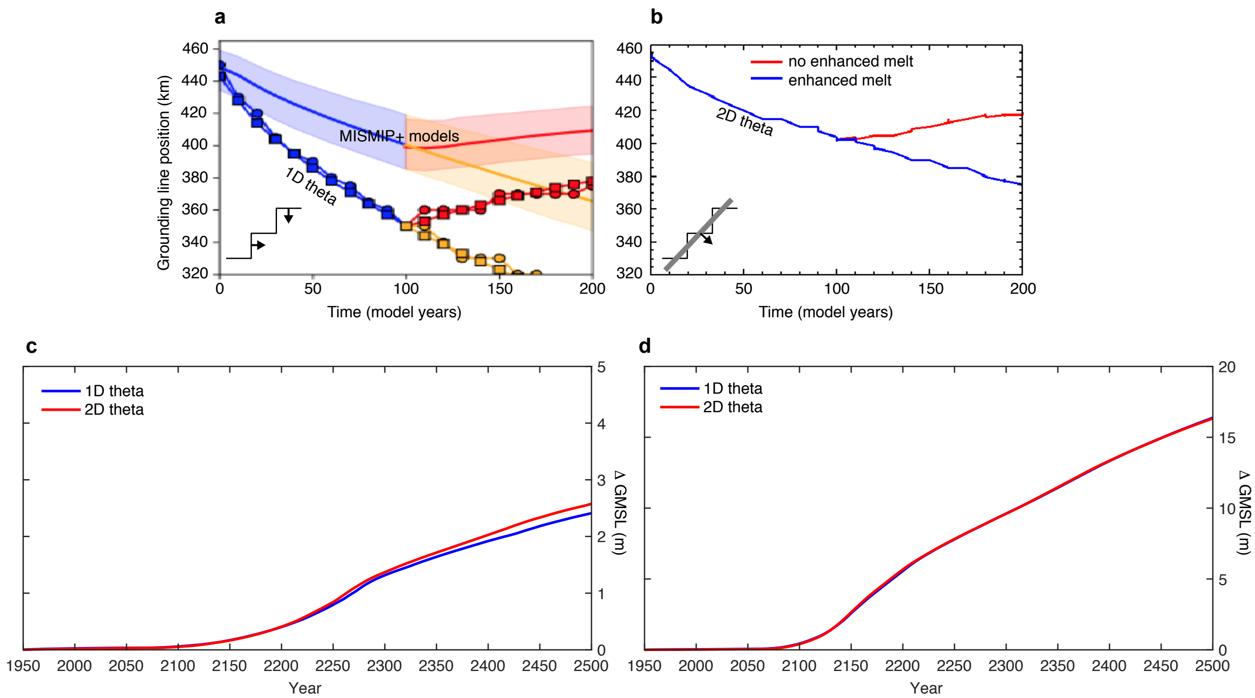

Supplementary Figure 4 | Effect of reformulated buttressing. a, Time-evolving, mid-channel grounding line position in Experiment Ice1 of the MISMIP+ model intercomparison[23], in an idealized, narrow fjord-like setting with reverse-sloped bedrock and channel width of 80 km (modified from Fig. 8b of ref.[24]). Blue and yellow colors show the response to oceanic basal melt rates applied at time 0, and red colors show the recovery after the basal melt rates are re-zeroed at year 100. Circles and squares show results of our standard model using the old θ method, with model resolution of 1 km and 10 km respectively. Shaded regions and solid lines show the envelope and mean of multiple other models in the MISMIP+ intercomparison (those using a similar Weertman-type basal sliding scheme). Our standard model retreats faster than other models in the intercomparison. **b,** Results with our model using the new, more rigorous θ method described above and 2-km model resolution. This substantially improves model performance relative to the other MISMIP+ models shown in **a**. Schematic diagrams representing the old versus new θ methods are shown at the bottom left of **a** and **b**, with the model grid represented by the thin black lines, arrows showing ice velocities across the grounding line, and the "actual" grounding line in the new method shown in grey. **c and d**, Continental-scale Antarctic simulations under RCP8.5 forcing, showing equivalent global mean sea level rise versus time corresponding to net Antarctic ice loss, without ice-cliff calving in **c**, and with ice-cliff calving in **d**. Unlike the idealized confined-fjord setting in **a** and **b**, these continental-scale Antarctic simulations show only small differences in net ice loss using the old vs. new θ methods. Without ice-cliff calving in **c**, the model using the new θ method (red curve) yields slightly faster ice loss after ~2300, but the differences are small and not important for the purposes of this paper. With ice-cliff calving in **d**, faster ice loss overwhelms any differences due to the θ method. The standard θ method (blue curves) is used in our main ensembles.

Statistical emulation of model ensembles

Here, we demonstrate the statistical robustness of the sea level estimates made with the ensembles presented in the main text. While the parameter sampling used in the ensembles is more dense than in our previous work[2], many parameter values intermediate to the training set (Table 1) have not been tested, and the sea level projections are not fully probabilistic (i.e. intermediate values are implicitly ascribed zero-probability). To address this, we develop and sample from an Antarctic Ice Sheet model emulator, which is continuous across the prior range of the training data and may be used to generate a much larger ensemble of simulations. We also evaluate the importance of observational (modern and paleo) constraints for limiting emulated probabilistic projections of future sea level rise from Antarctica.

Physically based and statistical emulation techniques have been used in several studies of sea level rise and climate change[25,26] and specifically to calibrate complex models[27,28]. Our methodology has similarities to the recent methods of ref.[29]. We use Gaussian Process (GP) regression[30] to construct a statistical emulator designed to mimic the behavior of the numerical ice-sheet model. GP regression is a non-parametric supervised machine learning technique which allows one to map model inputs (e.g., model parameters) to outputs (here, ice volume changes in global-mean sea level equivalent). In contrast to individual deterministic ice-sheet model simulations, GP regression is advantageous because the input parameter space and output prediction space are continuous, with emulation uncertainty inherently estimated for each output. For a set of untested inputs, the corresponding output and its uncertainty can be determined in a fraction of the time it takes to perform a single ice sheet model simulation. A full description and discussion of the emulator and its calibration are provided in a forthcoming manuscript[31].

The emulator is trained separately on two of the 196-member ensembles described in the main text: the Last Interglacial ensemble and the RCP8.5 scenario. We model the Antarctic ice-sheet contributions to global mean sea level (f) as the sum of two terms, each with a mean-zero Gaussian process prior:

$$f(\theta_1, \theta_2, t) = f_1(\theta_1, \theta_2) + f_2(\theta_1, \theta_2, t) \tag{S1}$$

The first term represents a parameter-specific intercept, the latter the temporal evolution of the contribution. The priors for each term are specified as:

$$f_1(\theta_1, \theta_2) \sim \mathcal{GP}(0, \alpha_1^2 K_1(\theta_1, \theta_2, \theta_1', \theta_2' \,; \ell_1)) \tag{S2}$$
$$f_2(\theta_1, \theta_2, t) \sim \mathcal{GP}(0, \alpha_2^2 K_2(\theta_1, \theta_2, \theta_1', \theta_2' \,; \ell_2) K_t(t, t' \,; \tau)) \tag{S3}$$

and where θ_1 is normalized VMAX, θ_2 is normalized CREVLIQ, α_i are amplitudes, ℓ_i are characteristic length scales in normalized parameter spaces, τ is the time scale and K is a specified correlation function. Because the LIG training data is evaluated at a single time point, there is no temporal term and f_2 is excluded in the LIG emulator construction. Each K_i is defined to be a Matérn covariance function with a specified smoothness parameter, $\gamma = 5/2$, which governs how responsive the covariance function is to sharp changes in the training data[30].

Optimal hyperparameters (α_i , ℓ_i, and τ) of the GP model are found by maximizing the log-likelihood, given the training simulations (Supplementary Table 1). The optimized model can then be conditioned on the training data to predict LIG and RCP8.5 simulation results for parameter values intermediate to those run with the full ice sheet model.

Taking uniform priors over the input parameters that are consistent with those used by the numerical ice sheet model (i.e., CREVLIQ ~ $U(0,195)$, VMAX ~ $U(0,13)$) we then apply a Bayesian updating approach to estimate posterior probability distributions for these parameters, conditional upon observational constraints. To do this, we first take 20,000 Latin Hypercube samples from the prior distributions, then weight these based on two different constraints: a uniform LIG distribution, $U(3.1\ \mathrm{m}, 6.1\ \mathrm{m})$, and a uniform distribution of IMBIE[32] trends, $U(0.15\ \mathrm{mm\ yr^{-1}}, 0.46\ \mathrm{mm\ yr^{-1}})$, over 1992-2017. As in the main text, the LIG constraint is based on the maximum Antarctic ice loss between 129 ka and 128 ka, equivalent to the ice loss at 128 ka. The results are posterior probabilities of CREVLIQ/VMAX pairs for each given constraint.

These posteriors of CREVLIQ/VMAX are then used to estimate the posterior distributions of AIS sea-level contributions over time. The 5th, 50th, and 95th percentiles of these posterior distributions (in 2100 under RCP8.5) with no constraints, IMBIE constraints only, LIG constraints only, and combined IMBIE and LIG constraints are presented in Supplementary Table 2. The probability distribution over time from 20,000 samples of the combined (IMBIE and LIG) constrained emulator is shown in Supplementary Figure 5b. In Supplementary Figure 6 we show the emulated probability distributions in 2100, subject to each constraint and compared to a histogram of the training set.

We note that the emulation results provided here are not directly comparable to the calibrated ensembles in the main text, because those ensembles add a third training constraint based on Pliocene sea level. Rather, these results are intended to complement the main paper by comparing projections that ignore the Pliocene constraints, and to demonstrate that statistically robust GP emulation compares favorably to the binary scoring approach used in Figure 1.

Emulated distributions closely resemble that of the 196-member training ensemble, with some notable but minor differences that are ascribable to sampling limitations in the original ensemble (e.g., the conditioned training ensemble has 10 simulations at or below its 5th percentile, whereas the constrained ensemble has 1000). As with the training ensemble, the emulated probability distribution without constraints is positively skewed, with a long upper tail that stretches to 63 cm in the 95th percentile by 2100.

We find that the prior distribution (Supplementary Figure 6) is qualitatively similar to the IMBIE-constrained distribution, and likewise the LIG-constrained distribution is similar to the IMBIE+LIG-constrained distribution. These results indicate that the IMBIE uniform distribution is not an adequately restrictive constraint on the emulator, although it does slightly reduce the upper bound of projections in 2100 by ~3 cm, shifting the distribution towards lower sea-level contributions. The IMBIE-constrained emulator is consistent with the conclusions of ref.[33] that additional information from the satellite record is of limited utility (because simulated ice-mass losses by the end of the 21st century are only weakly correlated with loss trends at the beginning of the 21st century).

In contrast, the uniform LIG constraint is more informative for calibrating emulated future projections of Antarctic sea-level contributions. Samples from parameter sets with CREVLIQ<45 and VMAX<4 fall outside the uniform LIG constraint, and the associated likelihoods are near or actually zero (not shown). Conversely, the VMAX/CREVLIQ parameter pairs above these values have greater (non-zero) likelihoods and the associated samples (which typically have higher RCP8.5 emulated sea-level contributions) are accordingly given more weight in the posterior. The resulting posterior distribution shifts towards the high end of the projections, with median projections in 2100 of 34 cm for the LIG-only constraint and 32 cm for the combined constraint distribution. Furthermore, the LIG-constrained distribution posterior has a narrower range than the prior starting in ~2060 and through 2100 (Supplementary Figure 5), demonstrating that future projections are less uncertain when the LIG constraint is applied.

Importantly, we find the median of GP emulation results is within 1 cm of the projected GMSL contribution in 2100 when compared to the training ensemble (binary scoring) approach used in the main text (Supplementary Table 2, Extended Data Figure 4). The addition of a third training constraint (Pliocene sea level) in the main text slightly increases the central estimate of Antarctica's GMSL contribution in 2100 from 32 cm (Supplementary Table 2) to 34 cm (Table 1), by further reducing the likelihood of both low and high VMAX/CREVLIQ parameter values.

Supplementary Table 1 | Optimized hyperparameters of the GP emulator found by maximizing the log-likelihoods, given the training ensembles

Ensemble	α_1^2 (m^2)	ℓ_1	α_2^2 (m^2)	ℓ_2	τ (yr)
LIG	2.823	0.3388	---	---	---
RCP8.5	0.03412	0.9002	1.014	1.427	54.77

Supplementary Table 2 | The median and 5th / 95th percentiles of projected Antarctic ice-sheet contributions to GMSL in 2100 (m)

Method	Constraint	5th Percentile	Median	95th Percentile
Emulator	None	0.05	0.28	0.63
Emulator	LIG: $U(3.1\ \mathrm{m}, 6.1\ \mathrm{m})$	0.08	0.34	0.66
Emulator	IMBIE: $U(0.15\ \frac{\mathrm{mm}}{\mathrm{yr}}, 0.46\ \frac{\mathrm{mm}}{\mathrm{yr}})$	0.05	0.25	0.59
Emulator	LIG + IMBIE	0.08	0.32	0.61
Training Ensemble	None	0.05	0.27	0.63
Training Ensemble	LIG + IMBIE	0.07	0.32	0.63

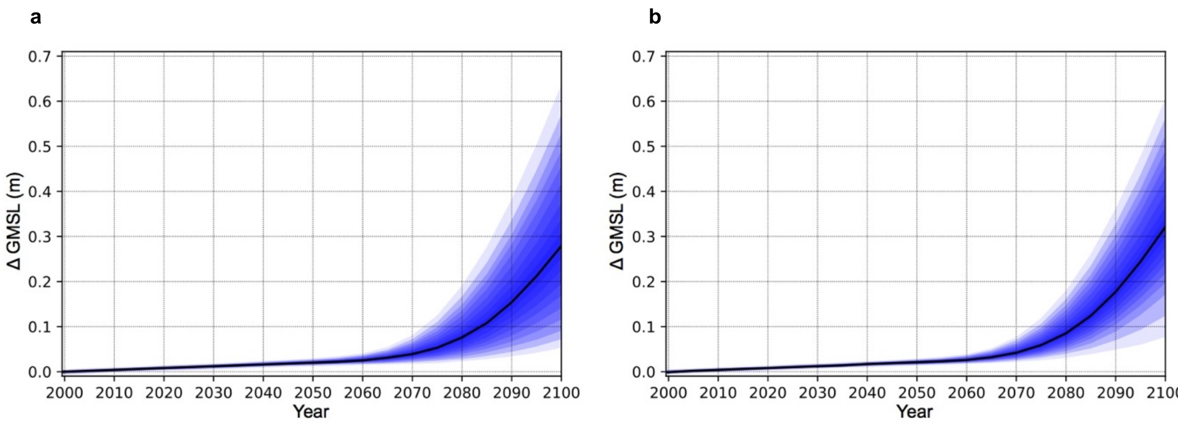

Supplementary Figure 5 | Emulated global mean sea level contributions from Antarctica. Fan charts of the range around the median (black line) in 10% increments from 20,000 RCP8.5 scenario emulator samples, from **a** the prior and **b** the posterior calibrated with combined LIG and IMBIE trend constraints using a Bayesian updating approach.

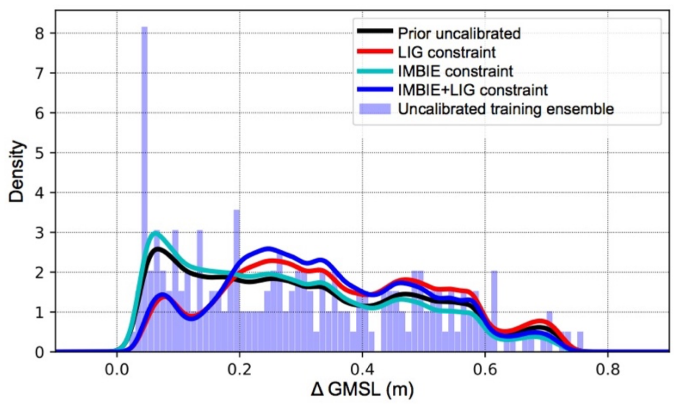

Supplementary Figure 6 | Probabilistic projections of global mean sea level contributions from Antarctica in 2100 under RCP8.5. Projections from 20,000 emulator samples (lines) weighted by different observational constraints. Shown are the prior distribution with no constraints (black), and distributions under the LIG uniform constraint (red), the IMBIE trend uniform constraint (cyan), and the combined LIG and IMBIE trend constraints (blue). Emulated distributions are shown using a kernel density estimation assumes a Silverman bandwidth divided by 2 (to prevent over-smoothing)[34]. The training ensemble from the main text is shown as a histogram (light blue) scaled for comparison to the emulated distributions.

References

1 DeConto, R. M. & Pollard, D. Contribution of Antarctica to past and future sea-level rise. *Nature* **531**, 591-597 (2016).

2 Trusel, L. D. *et al.* Divergent trajectories of Antarctic surface melt under two twenty-first-century climate scenarios. *Nature Geoscience* **8**, 927-932 (2015).

3 Eyring, V. *et al.* Overview of the coupled model intercomparison project phase 6 (cmip6) experimental design and organization. *Geosci. Model Dev.* **9**, 1937-1958 (2016).

4 Van den Broeke, M. R. Depth and density of the Antarctic firn layer. *Arctic, Antarctic, and Alpine Research* **40**, 432–438 (2008).

5 van Wessem, J. M. *et al.* Updated cloud physics in a regional atmospheric climate model improves the modelled surface energy balance of Antarctica. *The Cryosphere* **8**, 125-135 (2014).

6 Lenaerts, J. T. M., Vizcaino, M., Fyke, J., van Kampenhout, L. & van den Broeke, M. R. Present-day and future Antarctic ice sheet climate and surface mass balance in the Community Earth System Model. *Climate Dynamics* **47**, 1367-1381 (2016).

7 Tsai, C.-Y., Forest, C. E. & Pollard, D. The role of internal climate variability in projecting Antarctica's contribution to future sea-level rise. *Climate Dynamics* **55**, 1875-1892 (2020).

8 Ritz, C., Fabre, A. & Letreguilly, A. Sensitivity of a Greenland ice sheet model to ice flow and ablation parameters: Consequences for the evolution through the last climate cycle. *Climate Dynamics* **13**, 11-24 (1997).

9 Hazeleger, W. *et al.* Ec-earth v2.2: Description and validation of a new seamless earth system prediction model. *Climate Dynamics* **39**, 2611-2629 (2012).

10 Gent, P. R. *et al.* The Community Climate System Model version 4. *Journal of Climate* **24**, 4973–4991 (2011).

11 Long, M. C., Lindsay, K., Peacock, S., Moore, J. K. & Doney, S. C. Twentieth-century oceanic carbon uptake and storage in CESM1(BGC). *Journal of Climate* **26**, 6775-6800 (2013).

12 Meehl, G. A. *et al.* Climate change projections in CESM1(CAM5) compared to CCSM4. *Journal of Climate* **26**, 6287-6308 (2013).

13 Bentsen, M. *et al.* The Norwegian Earth System Model, NOResm1-M-Part 1: Description and basic evaluation of the physical climate. *Geosci. Model Dev.* **6**, 687-720 (2013).

14 Sadai, S., Condron, A., DeConto, R. & Pollard, D. Future climate response to Antarctic ice sheet melt caused by anthropogenic warming. *Science Advances* **in press** (2020).

15 Hersbach, H. *et al.* The ERA5 global reanalysis. *Quarterly Journal of the Royal Meteorological Society* **146**, 1999-2049 (2020).

16 O'Neill, B. C. *et al.* The Scenario Model Intercomparison Project (ScenarioMIP) for CMIP6. *Geosci. Model Dev.* **9**, 3461-3482 (2016).

17 Rignot, E., Mouginot, J., Morlighem, M., Seroussi, H. & Scheuchl, B. Widespread, rapid grounding line retreat of Pine Island, Thwaites, Smith, and Kohler glaciers, West Antarctica, from 1992 to 2011. *Geophysical Reseach Letters* **41**, 3502-3509 (2014).

18 Fürst, J. J. *et al.* The safety band of Antarctic ice shelves. *Nature Climate Change* **6**, 479 (2016).

19 Robel, A. A. & Banwell, A. F. A speed limit on ice shelf collapse through hydrofracture. *Geophysical Research Letters* **46**, 12092-12100 (2019).

20 Pollard, D. & DeConto, R. Description of a hybrid ice sheet-shelf model, and application to Antarctica. *Geoscientific Model Development* **5**, 1273-1295 (2012).
21 Schoof, C. Marine ice-sheet dynamics. Part 1. The case of rapid sliding. *Journal of Fluid Mechanics* **573**, 27-55 (2007).
22 Gudmundsson, G. H. Ice-shelf buttressing and the stability of marine ice sheets. *The Cryosphere* **7**, 647-655 (2013).
23 Pollard, D. & DeConto, R. M. Improvements in one-dimensional grounding-line parameterizations in an ice-sheet model with lateral variations. *Geophysical Model Development* **in press** (2020).
24 Cornford, S. L. *et al.* Results of the third Marine Ice Sheet Model Intercomparison Project (MISMIP+). *The Cryosphere Discuss.* **2020**, 1-26 (2020).
25 Levermann, A. *et al.* Projecting Antarctic ice discharge using response functions from searise ice-sheet models. *Earth System Dynamice* **5**, 271-293 (2014).
26 Nauels, A., Meinshausen, M., Mengel, M., Lorbacher, K. & Wigley, T. M. L. Synthesizing long-term sea level rise projections – the magicc sea level model v2.0. *Geosci. Model Dev.* **10**, 2495-2524 (2017).
27 Bastos, L. S. & O'Hagan, A. Diagnostics for gaussian process emulators. *Technometrics* **51**, 425-438 (2009).
28 Kennedy, M. C. & O'Hagan, A. Bayesian calibration of computer models. *Journal of the Royal Statistical Society: Series B (Statistical Methodology)* **63**, 425-464 (2001).
29 Edwards, T. L. *et al.* Revisiting Antarctic ice loss due to marine ice-cliff instability. *Nature* **566**, 58-64 (2019).
30 Rasmussen, C. E. & Williams, C. K. Gaussian processes for machine learning, vol. 1. *MIT press* **39**, 40-43 (2006).
31 Gilford, D. M. *et al.* Could the last interglacial constrain projections of future Antarctic ice mass loss and sea-level rise? *Journal of Geophysical Research: Earth Surface* **125**, e2019JF005418 (2020).
32 Shepherd, A. *et al.* Mass balance of the Antarctic Ice Sheet from 1992 to 2017. *Nature* **558**, 219-222 (2018).
33 Kopp, R. E. *et al.* Evolving understanding of Antarctic ice-sheet physics and ambiguity in probabilistic sea-level projections. *Earth's Future*, 1217-1233 (2017).
34 Silverman, B. W. *Density estimation for statistics and data analysis*. (Chapman & Hall, 1986).